KANSAS GEOLOGICAL SURVEY
OPEN-FILE REPORT 88-42

A Shallow Seismic Reflection Study of the Meers Fault
Comanche County, Oklahoma

by

Paul B. Myers

KANSAS GEOLOGICAL SURVEY
1930 Constant Avenue
University of Kansas
Lawrence, KS 66047

A Shallow Seismic Reflection Study of the Meers Fault

Comanche County, Oklahoma

by

Paul B. Myers

B.S. Lehigh University, 1986

Submitted to the Department of
Geology and the Faculty of the
Graduate School of the University
of Kansas in partial fulfillment
of the requirements for the degree
of Master of Science.

_____
Committee Chairman

_____

_____

_____
For the Department

_____
Date thesis accepted

TABLE OF CONTENTS

	Page
Acknowledgements	ii
Abstract	iv
List of Figures	vi
Introduction	1
Location and Purpose	2
Geologic Background	5
Structure	5
Tectonic Setting	7
Stratigraphy	10
Seismic Theory	11
Common Depth Point (CDP) Method	12
Resolution	14
Data Acquisition	16
Topography	25
Data Processing	27
Discussion	29
Results and Conclusions	65
References	68
APPENDIX:A Stratigraphy of Southwestern Oklahoma	71
APPENDIX:B Data Acquisition Parameters	77
APPENDIX:C Data Processing	78
APPENDIX D Complex Trace Analysis	80
APPENDIX:E Migration	85

ACKNOWLEDGEMENTS

I would like to begin by thanking my committee chairman Dr. Don W. Steeples for giving me the opportunity to come to Kansas. Don's policy at the survey enabled me to get involved in several interesting projects outside of my thesis. He was always willing to answer questions or make suggestions pertaining to my work. Don's reputation is what brought me to KU and I must say I wasn't the least bit disappointed after arriving. In addition I'd like to thank my other committee members Dr. Don Sprowl and Dr. Doug Walker. Don was extremely easy to work with and always seemed interested in what I was doing. I'd also like to thank him for his dedication in the classroom. Thanks goes to Doug Walker for keeping me in line geologically. His structural geology expertise helped significantly in making the interpretations in this thesis consistent.

I'd like to thank Rick Miller for taking charge of the acquisition and giving helpful suggestions during processing. Rick's field efficiency made everyone involved in acquisition's life a lot easier. Thanks goes to Jeff Treadway, Greg Hildebrand, Andrew Kalik, Randie Grantham, George Coyle, and Mary Anne Markezich for their help in the

field and friendship. I'd like to thank Brett Bennett, Dao Somanas, and Young Chung for their help with the migration aspects of this thesis.

Last but certainly not least, I'd like to thank my fiance Tonja. If it weren't for her I probably would have finished writing a year ago, however, I'd probably still be sitting at the typewriter.

ABSTRACT

A high-resolution seismic survey in the vicinity of the Meers Fault Scarp in Comanche County Oklahoma was conducted to achieve a better understanding of the shallow structure associated with the fault zone. Three reflection profiles were acquired using a downhole .50-caliber rifle as the seismic energy source and two 100-Hz geophones connected in series at each receiving station. Two profiles (seismic lines 1 and 2) were oriented perpendicular to the scarp and one profile (seismic line 3) was oriented parallel to the scarp. Field parameters were set to optimize the recording of seismic reflections in the 40 to 150 ms range. Pre-analog-to-digital filters applied during recording helped increase the dominant reflection frequencies into the 100 to 250 Hz range. Reverse faulting is evident on the fault associated with the scarp as well as throughout a line extending 250 meters southwest to 200 meters northeast of the scarp. The high quality stacked CDP seismic data allows interpretation of an up-to-the-north vertical to high-angle reverse slip orientation on the Meers Fault. Quantification of most recent vertical displacement on the fault associated with the scarp requires drill-core data. Maximum vertical displacement does not exceed 10 meters on the remainder of the secondary interpreted faults. Normal faulting dominates the seismic

data of line three acquired parallel to the scarp. A graben with maximum displacement of approximately 10 to 30 meters is the major feature on the stacked CDP section. Deformation is apparent throughout the line suggesting strike slip motion along the fault may have resulted in deformation along its entire length. The instantaneous phase and instantaneous frequency complex trace attributes of the seismic traverses support the interpreted fault structures. The evidence supporting strike slip motion in conjunction with high-angle up-to-the-north reverse faulting places the Meers Fault in a transpressive tectonic environment during Quaternary time.

LIST OF FIGURES

FIGURE		PAGE
1.	Tectonic setting of the Meers Fault	3
2.	Location map of the study area	4
3.	Major tectonic subdivisions of Oklahoma	8
4.	Common depth point (CDP) method	13
5.	Location of seismic line 1	18
6.	Walkaway noise test-line 1	20
7.	Location of seismic lines 2 and 3	21
8.	Walkaway noise test-line 2	22
9.	Walkaway noise test-line 3	24
10.	Relative elevation of lines 1 and 2	26
11.	Relative elevation of line 3	28
12.	Representative field files-line 1	31
13.	Final CDP stacked section-line 1	35
14	Horizontal oversampling phenomenon (line 1)	36
15.	Instantaneous frequency section-line 1	39
16.	Instantaneous phase section-line 1	41
17.	Interpretive line drawing-line 1	42
18.	Representative field files-line 2	44
19.	Final CDP stacked section-line 2	48
20.	Instantaneous phase section-line 2	51
21.	Instantaneous frequency section-line 2	53
22.	Interpretive line drawing-line 2	54
23.	Representative field files-line 3	56

24. Final CDP stacked section-line 3 57

25. Instantaneous phase section-line 3 59

26. Instantaneous frequency section-line 3 60

27. Brute stack with vel=1250 m/s-line 3 61

28. Brute stack with vel=2000 m/s-line 3 62

29. Interpretive line drawing-line 3 64

30. Stratigraphic section of southwestern Oklahoma 75

31. Representation of the complex seismic trace 81

32. Migration of a segment of a dipping event 86

33. Flow chart for $f-k$ migration 88

34. 2D Fourier Transform to the $f-k$ plane 89

35. Procedure for $f-k$ migration 91

36. Migrated section-line 1 93

INTRODUCTION

The Meers Fault, located in southwestern Oklahoma, marks the northern boundary of the Wichita Uplift, and is one of the few known active faults in the mid-continental region. According to Ramelli et al. (1986) the fault appears to conform to a uniform compressional tectonic regime that encompasses almost the entire central and eastern United States as outlined by Zoback and Zoback (1980). Several regional geophysical studies of this area reveal the general orientation of the fault but lack the resolution to thoroughly decipher the detailed structure.

The evidence for Quaternary tectonic activity has resulted in an ever increasing interest among geoscientists to understand the orientation and driving mechanisms of this mid-continent fault zone. Informative outcrop along the Meers Fault scarp is scarce and a turn to subsurface geophysical methods is necessary in order to delineate the structural picture of the fault zone.

High-resolution shallow seismic reflection has only recently been introduced as a method for detailed fault delineation (Treadway et al., 1985; Treadway et al., 1988; Miller and Steeples, 1986). Shallow seismic reflection is relatively inexpensive and quick, and has proven to be a valuable technique for understanding fault systems.

Shallow reflection techniques are used in this thesis to enhance the understanding of the shallow subsurface geology associated with the Meers Fault.

LOCATION AND PURPOSE

The Meers Fault marks the southern boundary of the Wichita Frontal Fault system separating the Wichita Uplift to the south, and the Anadarko Basin to the north (Figure 1). The site chosen for this study is located in Comanche County, Oklahoma, section 24, T4S, R13W, on the Meers, Oklahoma 15 minute quadrangle (Figure 2). The location was chosen in consultation with geologists at the Oklahoma Geological Survey to eventually coordinate this study with a trenching and drilling project proposed by the Oklahoma Survey.

The purpose of this study was to identify and interpret the shallow (approximately upper 200 meters) structural features associated with the Meers Fault in Comanche County, Oklahoma, using high-resolution reflection seismology. This was accomplished by collecting common depth point (CDP) seismic reflection data over the fault zone, processing the CDP seismic data, and analyzing and interpreting the individual seismic sections. In addition,

Figure 1. Tectonic setting of the Meers Fault. The Meers Fault is the southern most fault in the Wichita Frontal Fault System separating the Anadarko Basin to the north and the Wichita Uplift to the south.

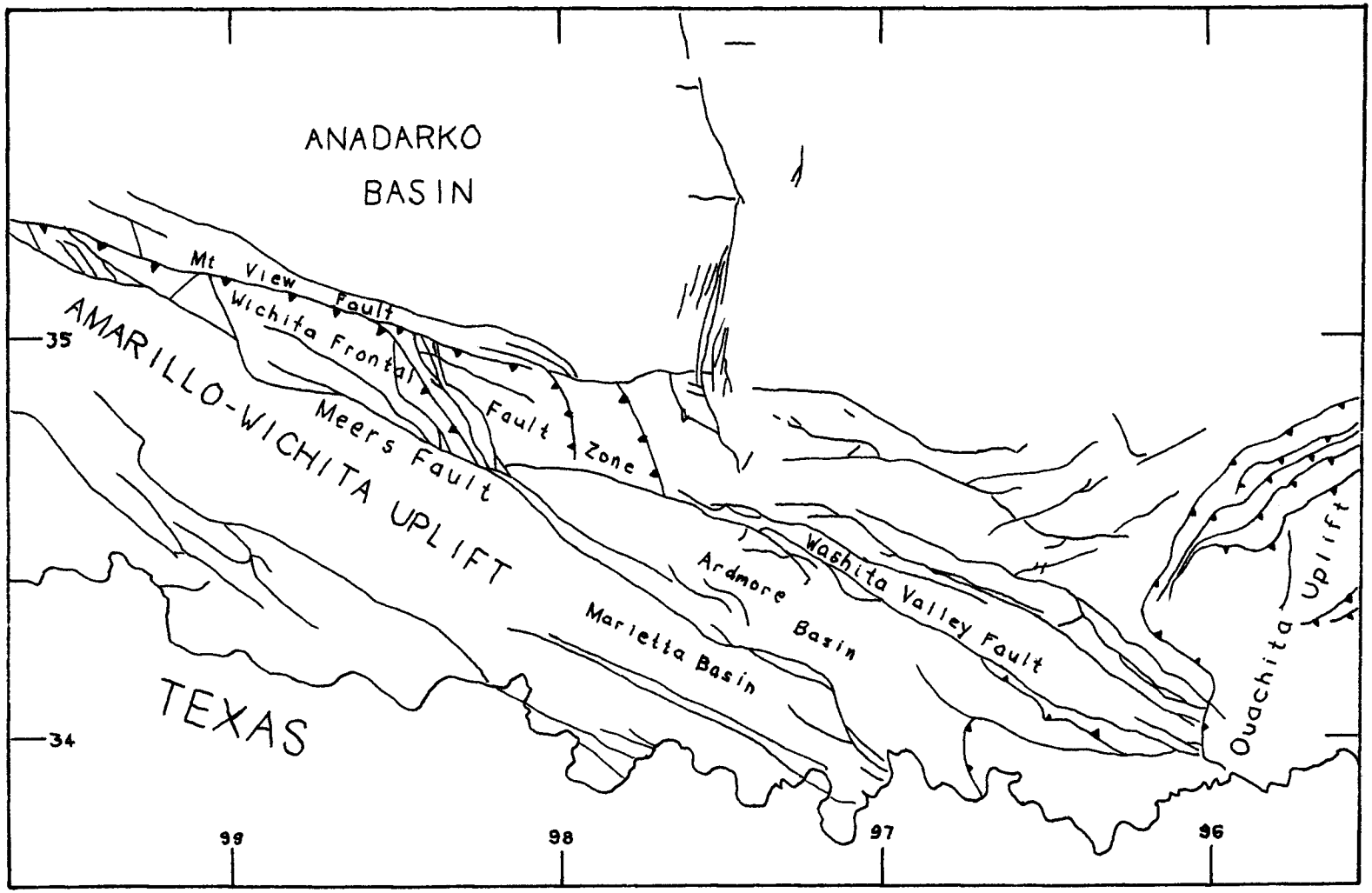
ANADARKO
BASIN
Mt View Fault
Wichita Frontal
Fault Zone
Meers Fault
AMARILLO-WICHITA UPLIFT
Ardmore Basin
Marietta Basin
Washita Valley Fault
Ouachita Uplift
TEXAS
35
34
99
98
97
96

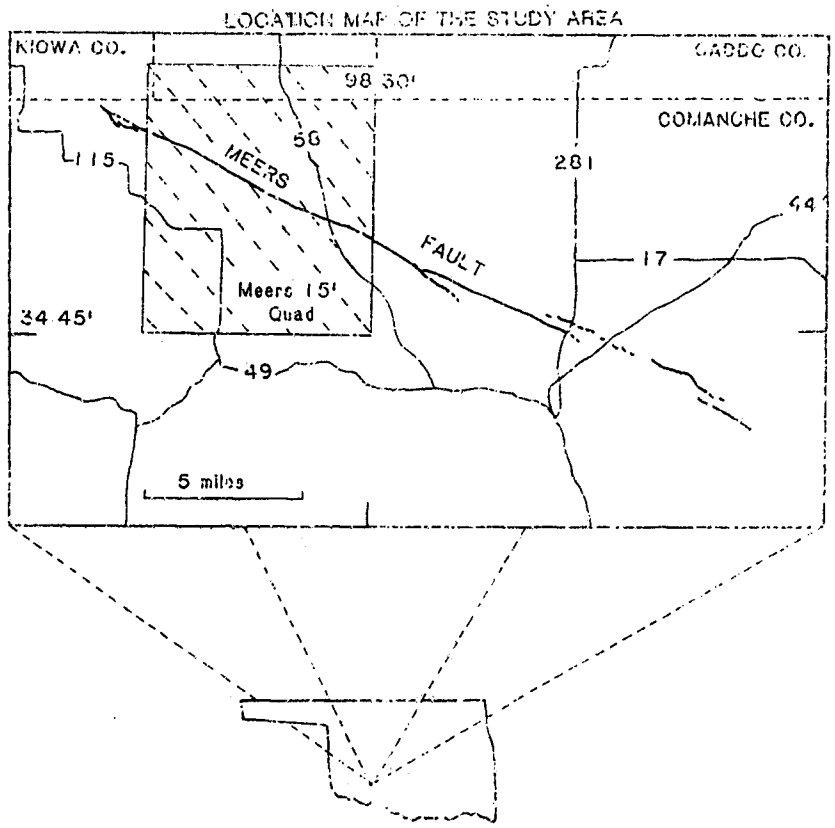

Figure 2. Location map of the study area in the Meers, Oklahoma 15 Minute Quadrangle, Section 24, T4S, R13W, Comanche County Oklahoma.

a goal of this study was to achieve a better understanding of what data processing techniques produce the best overall picture of the shallow subsurface geology.

GEOLOGIC BACKGROUND

Structure

Harlton (1951) was the first to map the Meers Fault region. He recognized several miles of vertical displacement across the zone extending from the Wichita Mountains to the south into the subsiding Anadarko Basin to the north. Harlton believed the displacement occurred along a predominantly vertical fault system, with the Meers Fault representing the southern bounding fault in the system. On the basis of the present day surface expression of the Meers Fault, Harlton believed the fault was down-to-the-south. In later papers Harlton (1963, 1972), observed that the basement igneous complex to the south is in close proximity to the basin sediments to the north, and concluded that this relationship required considerable up-to-the-south displacement, altering his original interpretation on the the displacement along the fault. Harlton believed the several miles of displacement observed across the Wichita Mountains and the Anadarko Basin must be dispersed over several faults. He concluded that most

recent movement on the Meers Fault was down-to-the-south, however the relationship observed between the Wichita Uplift and the Anadarko Basin required that the majority of the motion along the Meers Fault since it formed was up to the south.

On the basis of COCORP seismic data, Brewer et al. (1983) suggested that the igneous complex to the south was brought in contact with the basin sediments to the north along southerly dipping thrusts. They interpreted the Mountain View Fault bounding the Anadarko Basin to the north as the major thrust fault dipping 30-40 degrees to the south, and inferred a similar orientation for the Meers Fault. Studies by Crone and Luza (1986), Ramelli and Slemmons (1986), and Ramelli et al. (1987), in conjunction with this study indicate a subvertical to northerly dipping orientation for the Meers Fault at the near surface (upper 200 meters). This evidence suggests that the thrusting hypothesis may be correct at depth, but the orientation steepens substantially and possibly overturns as the fault approaches the surface.

Trenching at two locations on the Meers Fault reveals the last movement to be reverse slip deformation (Crone and Luza, 1986). Carbon 14 dating in the displaced alluvium indicates the last movement occurred in late Holocene time (Crone and Luza, 1986) with maximum vertical displacement

of approximately 5 meters (Ramelli and Slemmons, 1986; Ramelli et al. 1987).

In addition to vertical displacement, studies by Donovan et al. (1982), Butler (1980), McLean and Stearns (1983), Ramelli and Slemmons (1986), and Ramelli et al. (1987), have demonstrated significant left lateral strike slip components of displacement associated with the Meers Fault. Evidence for strike slip deformation is displayed in wrench folds, horizontal slickensides, joint patterns, and fault displacements. Maximum horizontal displacement of the Holocene strike slip deformation appears to be approximately 25 m based on displaced Quaternary Alluvium deposits (Ramelli and Slemmons, 1986; Ramelli et al., 1987).

Tectonic Setting

The Meers Fault appears to be only part of a much larger structural feature known as the Amarillo-Wichita-Arbuckle Uplift (Figure 3). This region extends for several hundred kilometers from the Texas panhandle into Oklahoma, truncating in the eastern portion of the state. The recent activity on the Meers Fault may indicate a potential for activity along much if not all of the Amarillo-Wichita-Arbuckle Uplift.

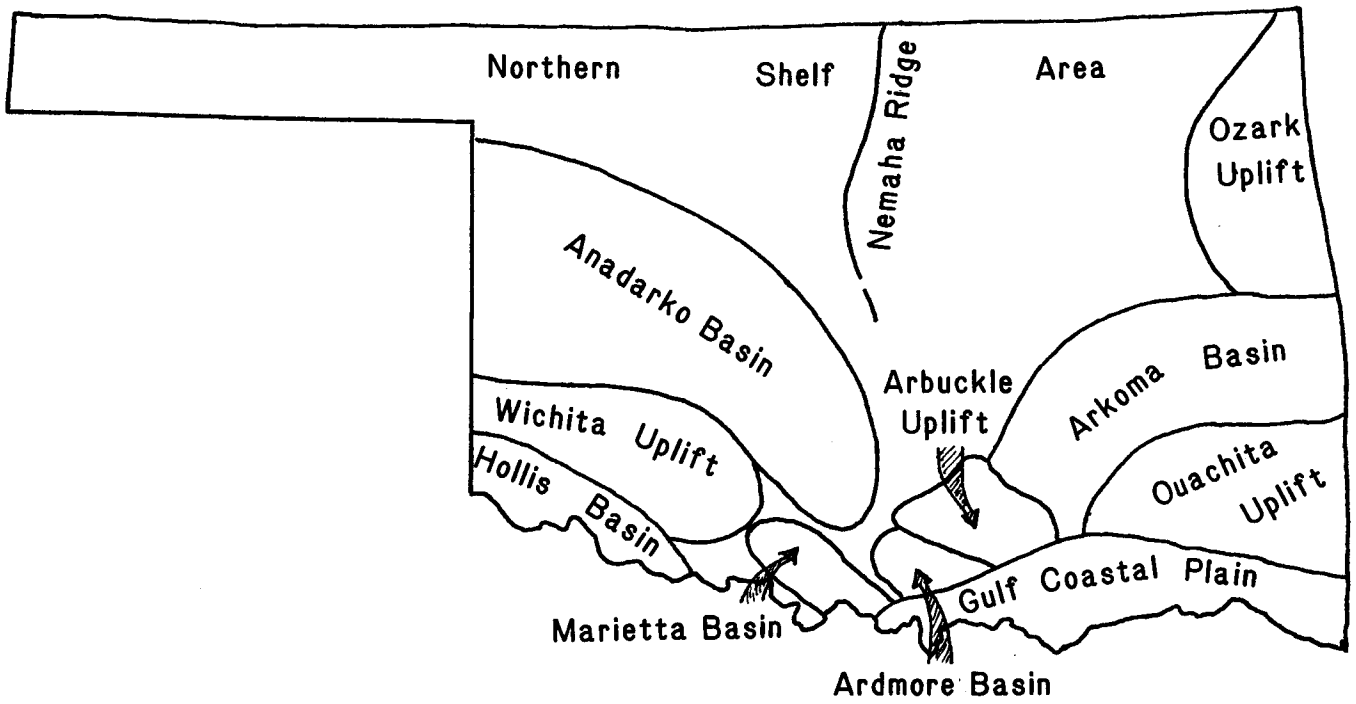

Figure 3. Major tectonic subdivisions of Oklahoma

Cox and Van Arsdale (1986) have suggested that recent activity has occurred on the Washita Valley Fault in the Arbuckle Mountains southeast of the Meers Fault. According to Ramelli and Slemmons (1987), the Washita Valley Fault resembles the Meers Fault in some features such as fault trend, a steep to moderate northward dip, exposure within resistant rock units, and up-to-the north displacement.

In addition, seismic activity near Enola, Arkansas has occurred along the northern edge of the Ouachita fold and thrust belt (Haar et al., 1984). The Ouachita fold and thrust belt truncates the Amarillo-Wichita-Arbuckle Uplift to the east. Haar (19834) has derived a composite focal mechanism from the seismic activity which is compatible with the left-lateral displacement for a plane of similar orientation to the Meers Fault.

These various pieces of evidence suggest that the Amarillo-Wichita-Arbuckle Uplift may have the potential for earthquakes along much of its length. Therefore stress regimes driving the motion in what was thought to be a portion of the stable craton need to be further studied. Advances in stress measurement techniques in the crust suggest that the entire central and eastern United States is subject to a uniform, horizontal compressive stress oriented ENE-WSW to NE-SW (Zoback and Zoback, 1980). The Meers Fault and Amarillo-Wichita-Arbuckle Uplift have WNW

trends. Given this orientation and the existing compressive stress field, left lateral strike-slip motion would be predicted. The left lateral nature has been observed on the Meers Fault (Ramelli and Slemmons, 1987), as well as supported by the composite focal mechanism for an earthquake swarm near Enola, Arkansas (Haar et al., 1983).

Stratigraphy

Pre-Paleozoic topography of the Wichita Mountains Anadarko Basin area consisted of small hills of rhyolite reaching heights of approximately 100 meters (Donovan and Ragland, 1986). The hills were part of the Carlton Rhyolite Group forming the upper part of the basement igneous complex.

The Paleozoic record consists of sediments deposited in early Cambrian time up through the Permian period. Early deposition consisted of predominantly a quartz sand in the Cambrian, but changed to carbonate deposition in the Ordovician. The majority of the Paleozoic record consists of carbonate rock with major amounts of carbonate mud. Interbedded with the carbonate deposits are some intraformational conglomerates and minor sandstones. The three depositional groups comprising the Paleozoic record are the Timbered Hills Group (Cambrian), the Arbuckle Group

(Late Cambrian-Late Ordovician), and the Hennessey Group (Permian). The Paleozoic sequence around this study area is overlain by a Holocene deposit known as the Porter Hill Alluvium. A more detailed account of the stratigraphy of southwestern Oklahoma can be found in APPENDIX A.

SEISMIC THEORY

Reflection seismology is the most widely used and most successful exploration geophysical technique. Seismic reflection techniques involve the input of an acoustic wave into the ground, usually via an artificial source. Typical seismic sources are explosives, vibroseis, weight drops, and projectiles shot from various caliber rifles. The energy produced by the source travels down into the subsurface where it reflects off geological layers back to the surface where it is detected by geophones. Geophones are velocity sensitive devices which convert ground motion into voltages which eventually are amplified, filtered, converted from analog to digital, and recorded in the field.

The percentage of energy reflected from a seismic discontinuity is determined by the contrast in acoustic impedance across the discontinuity. Acoustic Impedance (Z) is defined as the product of the density (ρ) and

velocity (v) of a given unit. The reflection coefficient (R) determines the percentage of energy reflected from a given interface. The reflection coefficient (R) for normally incident energy is defined as:

$$R = (Z_2 - Z_1)/(Z_2 + Z_1)$$

where:

Z_1 = acoustic impedance of the upper layer = $\rho_1 v_1$

Z_2 = acoustic impedance of the lower layer = $\rho_2 v_2$

Any contrast in acoustic impedance from one layer to the next results in some percentage of energy being reflected.

COMMON DEPTH POINT METHOD

The Common Depth Point method (CDP) is an acquisition technique that usually results in a large increase in the signal to noise ratio (S/N) (Mayne, 1962). The concept of the CDP method is illustrated in figure 4. The ray path diagram in figure 4 illustrates how different shot and receiver locations may have a common reflecting point in the subsurface. However, the geometrical difference in travel path length results in different arrival times for

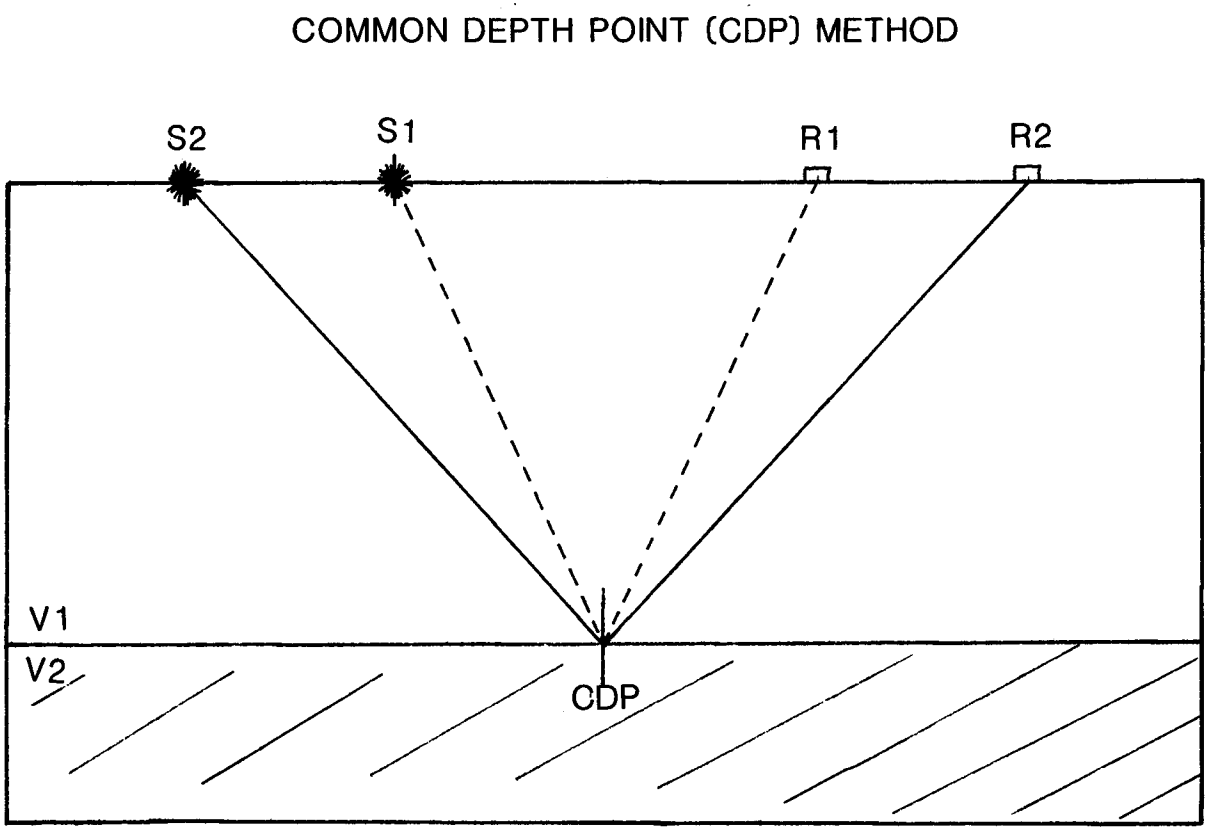

Figure 4. Illustration of the Common Depth Point (CDP) method.

reflected waves at each shot receiver pair. During processing the individual traces are time-adjusted for their differences in travel path length. Each trace is adjusted such that the reflected event arrives at the time (t_o) where it would arrive if the energy were vertically incident. This correction is known as the normal moveout process (NMO). Following normal moveout correction, the traces are summed together forming a single trace which displays an increase in signal (constructive interference) wherever there is coherent energy and a decrease in noise (destructive interference) due to the random nature of the noise. This method results in an increase in (S/N) that is proportional to the square root of the number of traces added.

RESOLUTION

Sheriff (1984) defines resolution as "the ability to separate two features which are very close together". The concept of resolution can be observed in both a vertical and a horizontal sense.

Vertical resolution deals with the ability to distinguish that more than one reflecting interface contributes to an observed reflection. The most common definitions of vertical resolvable limit come from Lord

Rayleigh, who studied resolution as applied to visible light, and Widess (1973). Vertical resolvable limits given by these two definitions are $\frac{1}{4}$ and $\frac{1}{8}$ of the dominant wavelength, respectively. For example, suppose the dominant wavelength of the seismic energy is approximately 160 meters. The minimum thickness bed that can be resolved according to Widess, is $\frac{1}{8}(160)$ or 20 m. Any unit less than 20 m thick will essentially go unnoticed.

Another important aspect of resolvability involves the wavelet bandwidth. According to Sheriff (1985), a seismic wavelet must have a bandwidth of at least one-and-a-half octaves to be reasonably compact and a broader bandwidth further improves the wavelet's shape. Efforts to improve resolvability by improved acquisition techniques concentrate on increasing the high frequency-content and hence increase the bandwidth.

Horizontal resolution is usually described in terms of the first Fresnel zone. Contrary to raypath representation of reflections, reflected energy does not come from a point, but represents a sampling from a relatively large area of the reflecting surface. This area is related to the first Fresnel zone which was first studied in optical physics. The radius of the first Fresnel zone depends on reflector depth (D) and wavelength (λ) of the reflected energy (Knapp and Steeples, 1986).

$$R \approx \sqrt{D\lambda/2}$$

Alternatively, the radius of the first Fresnel zone can be given as a function of seismic velocity (v), dominant frequency of the seismic energy (f), and two way reflection time (T), (Knapp and Steeples, 1986).

$$R \approx 0.5V\sqrt{T/f}$$

Frequency is the only variable in this form of the equation and therefore the radius of the first Fresnel zone can be reduced by acquiring higher dominant frequencies. Horizontal resolvable limit is usually taken as the diameter of the first Fresnel zone ($2R$).

DATA ACQUISITION

High-resolution CDP seismic-reflection data were collected from the study area in mid-December, 1986 and mid-March, 1988. A projectile fired from a modified .50-caliber rifle provided the seismic energy for both surveys. The rifle was mounted on a steel plate with the barrel lowered approximately .6 m down a 4 cm diameter augered hole. Lowering the barrel down a borehole diminishes the

effects of the air-coupled wave (the sound wave that travels from the source to the receivers through the air) and increases the overall amplitude of the recorded seismic energy (Steeples et al., 1987).

The first survey, collected in mid-December, consisted of a short CDP profile (hereafter referred to as line 1) perpendicular to the fault scarp (Figure 5). The data were collected using end-on source/receiver geometry (source located off the north end of the receiving geophones) with two 100-Hz geophones connected in series at each receiving station. Two geophones connected in series helped increase the signal amplitude slightly while cancelling small amounts of wind noise. End-on geometry was used in an attempt to achieve better velocity control. Receiver station spacings were set at 1.2 m intervals providing 12-fold coverage every 0.6 m in the subsurface. The relatively close geophone spacing was used in an attempt to maintain continuity of reflectors across the fault zone. The source spacing was twice the receiver spacing. Two shots were separately recorded at each shot point station while incrementing the receivers one receiver spacing for each shot. The above procedure resulted in two source to closest receiver distances of 29.3 m and 30.5 m respectively. This provided full subsurface coverage and cut the number of shot holes augered by 50%. The shot-to-

Figure 5. Location of seismic line 1 (perpendicular to the scarp).

SEISMIC LINE 1 LOCATION

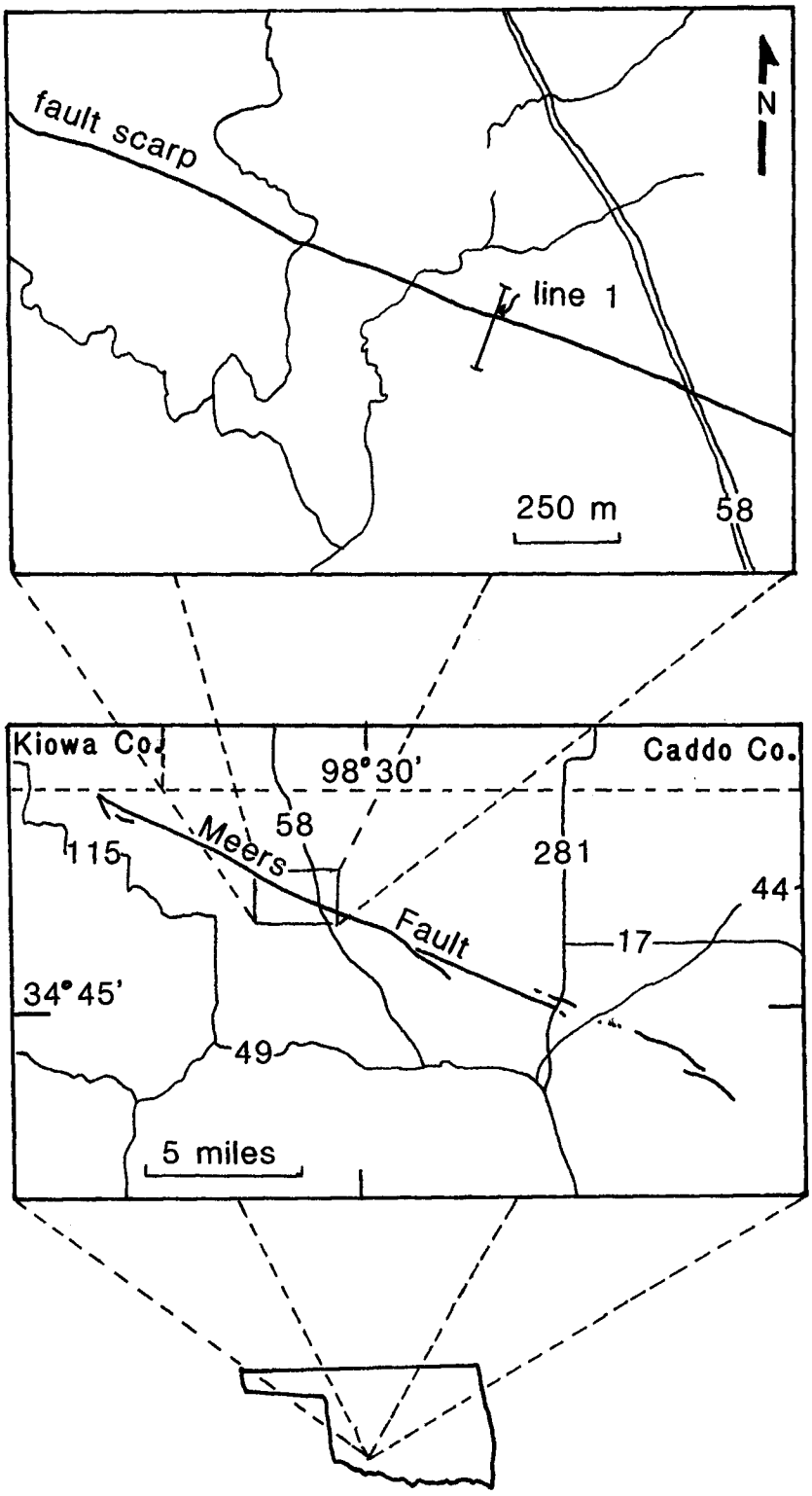

closest-receiver distances were determined with the use of a walkaway noise test (Figure 6). The noise test enables us to select the "optimum recording window" (Hunter et al., 1984).

The second survey, collected in mid-March, 1988, consisted of two CDP profiles. The first (hereafter referred to as line 2) oriented in the same direction as line 1 (Figure 7). The second (hereafter referred to as line 3) ran parallel to and approximately 20 m south of the scarp (Figure 7).

Data for line 2 were collected using end-on source/receiver geometry with two 100-Hz geophones connected in series at each receiving station. Receiver and shot station spacings were set at 2 m intervals providing subsurface coverage every 1 m. Two shots were individually recorded at each shot station. For the first shot, the 24 receiving stations were located off the southwest end of the source. For the second shot, the 24 receiving stations were located off the northeast end of the source. Selection of an "optimum recording window" through observation of a walkaway noise test, (Figure 8), resulted in a source to closest receiver distance of 20 m. A source-to-closest-receiver distance of 20 m for both directions resulted in a farthest offset of 66 m. Recording two shots, one in each direction, resulted in 24-

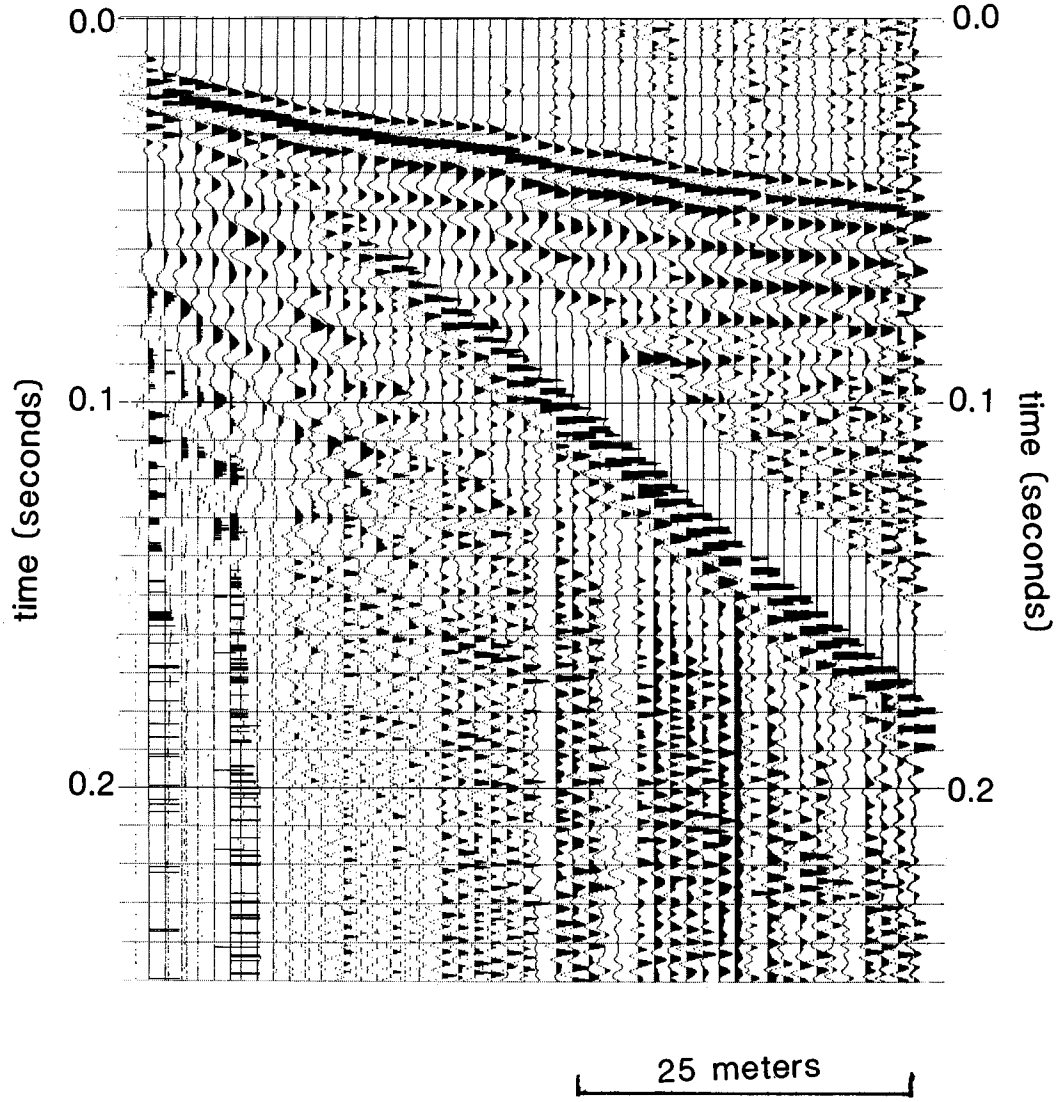

Figure 6. Walkaway noise test for seismic line 1 recorded with a 220 Hz low-cut (hi-pass) analog filter.

Figure 7. Location of seismic lines 2 and 3. (Line 2 is oriented perpendicular to the scarp and is an extension of line 1, and line 3 is oriented parallel to the scarp).

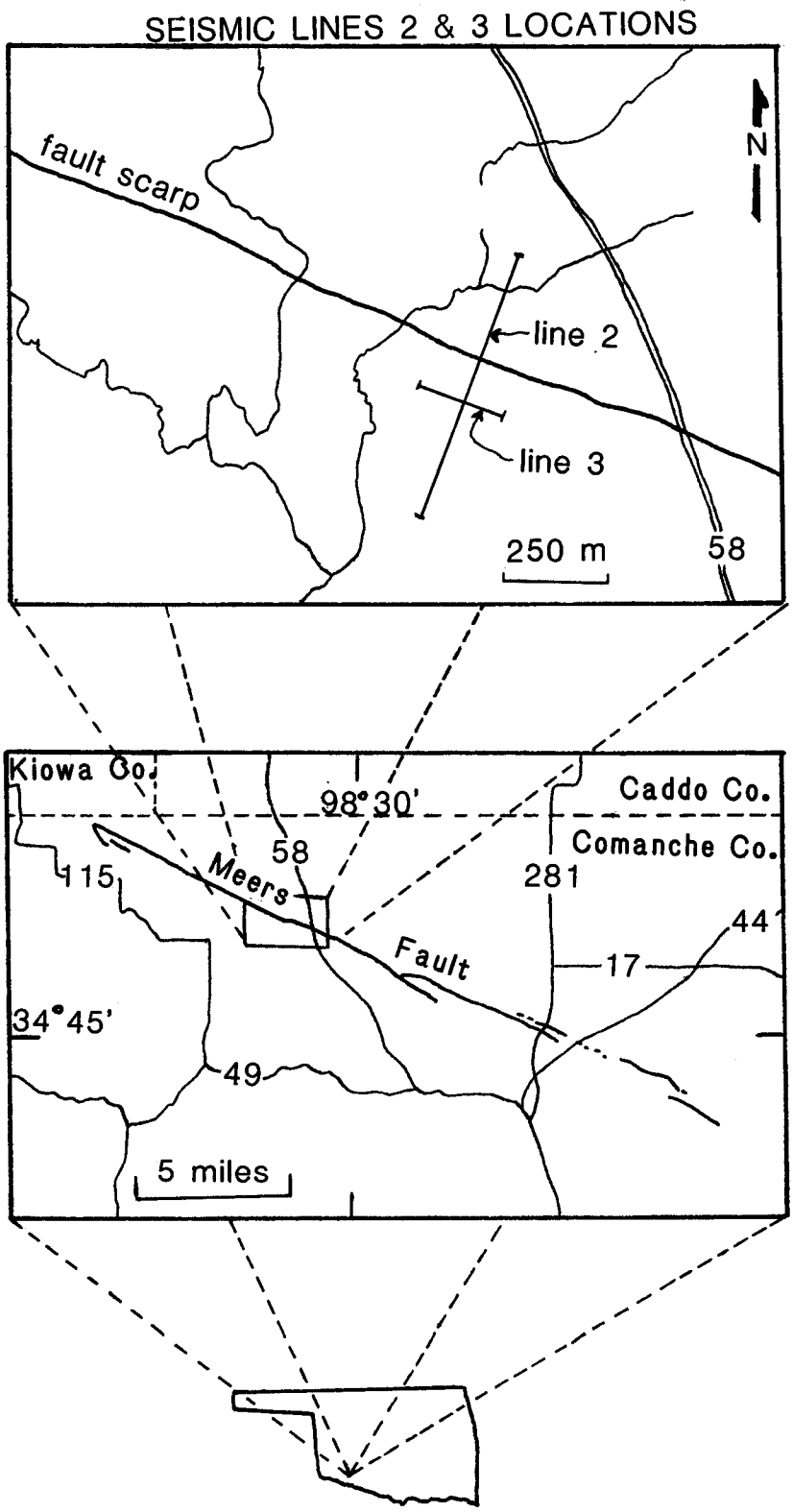
SEISMIC LINES 2 & 3 LOCATIONS
fault scarp
N
line 2
line 3
250 m
58
Kiowa Co.
98°30'
Caddo Co.
Comanche Co.
58
115
Meers
281
44
Fault
17
34°45'
49
5 miles

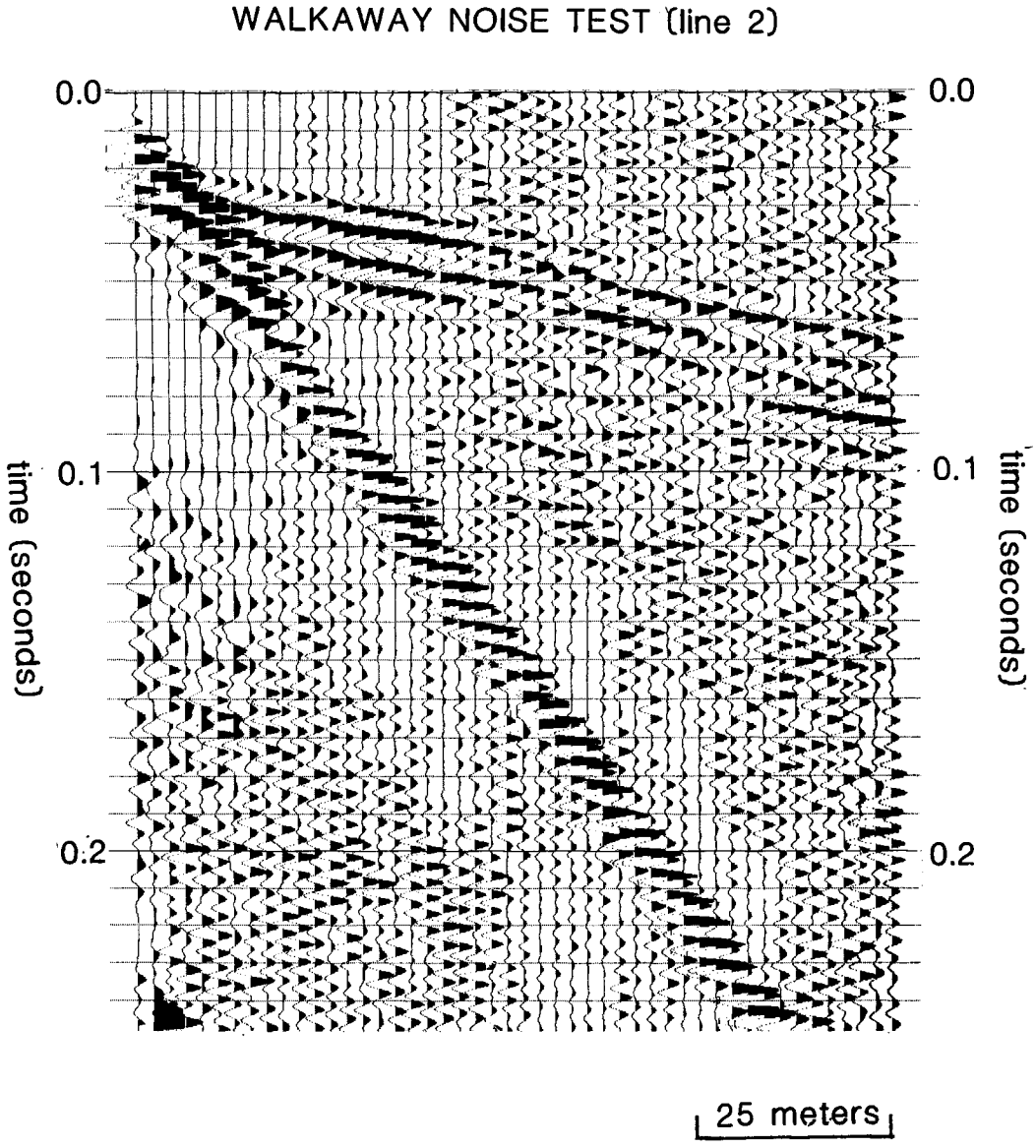

Figure 8. Walkaway noise test for line 2 recorded with a 220 Hz low-cut (hi-pass) analog filter. The S/N is significantly lower than observed on the walkaway for line 1.

fold coverage in the subsurface. In addition, this method provided a pseudo-split-spread geometry necessary for dip control in structurally complex studies, without sacrificing velocity control which would occur by decreasing the lateral coverage distance.

Data for line 3 were collected parallel to the scarp also using end-on source/receiver geometry with two 100 Hz geophones connected in series at each receiving station. Similar to line 2, receiver and shot spacings were both set at 2 m. One shot was recorded at each station providing 12-fold coverage every 1 meter in the subsurface. Observation of the walkaway noise test resulted in a source to closest receiver distance of 20 m (Figure 9). The source was located off the northwest end of the receiving stations-with farthest offset equal to 66 m.

An Input/Output, Inc. DHR-2400 seismic recording system was used to amplify, filter, convert from analog to digital, and record the data in the field. In order to increase the dominant reflection frequencies recorded in the field, analog low-cut (high-pass) filters were applied. Line 1 was recorded with a low-cut filter with 24 db/octave rolloff below the -3 db point of 220 Hz. Line 2 and 3 were both recorded with a low-cut filter with 24 db/octave rolloff below the -3 db point of 110 Hz. As a result, recorded reflection frequencies of the CDP data were

Figure 9. Walkaway noise test for line 3 recorded with a 110 Hz low-cut (hi-pass) analog filter. S/N improved significantly compared to the walkaway for line 2.

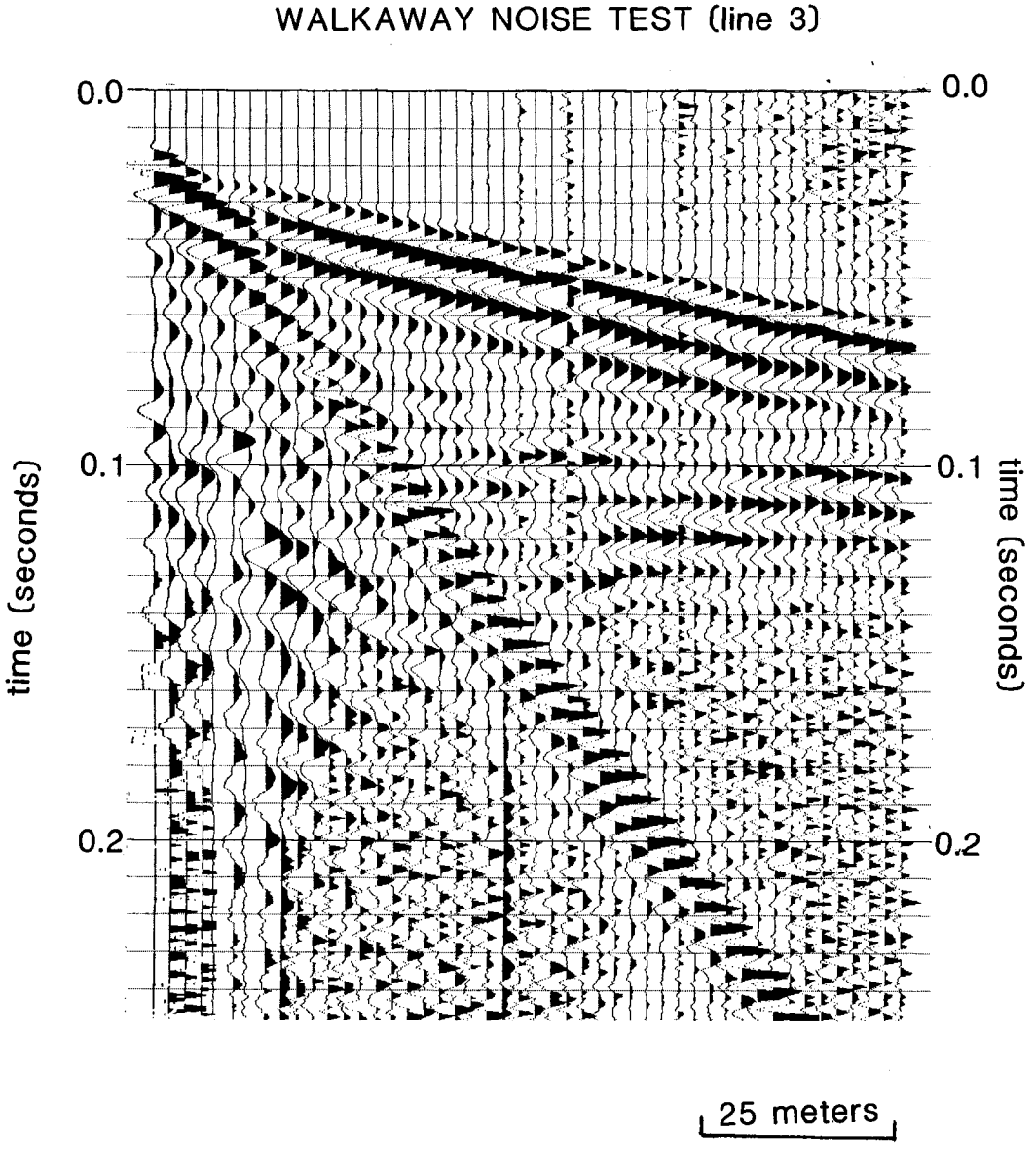
WALKAWAY NOISE TEST (line 3)
0.0
0.1
0.2
time (seconds)
0.0
0.1
0.2
time (seconds)
25 meters

increased. Assuming a percentage of low frequency energy was still present, the extended bandwidth resulted in increased vertical resolution. Recording parameters for the acquisition of all three seismic lines are listed in APPENDIX:B.

TOPOGRAPHY

Relative elevation data for all three seismic traverses were collected using a hand level and stadia rod. The resulting uncertainty for this method is approximately 15 cm.

The purpose in collecting elevation data is primarily to correct for time shifts in individual traces caused by differences in surface elevations and differences in the thickness of the weathered layer at the surface. These corrections are referred to as static corrections because the time shift applied is constant for the entire trace.

Relative elevation data for line 1 and line 2 are displayed in figure 10. Discussion of the topography of line 1 will be incorporated in the topographic discussion for line 2 since line 2 is merely an extension of line 1.

Total elevation change from the northeast to the southwest ends of the seismic traverse appears to be approximately six to seven meters. The regional slope on both the upthrown and downthrown portions of the line seems

Figure 10. Relative elevation data for seismic lines 1 and 2. The scarp is located between CDP 325 and 400 on line 1 and between CDP 440 and 380 on line 2. A stream channel is present between CDP 380 and 580 on line 2.

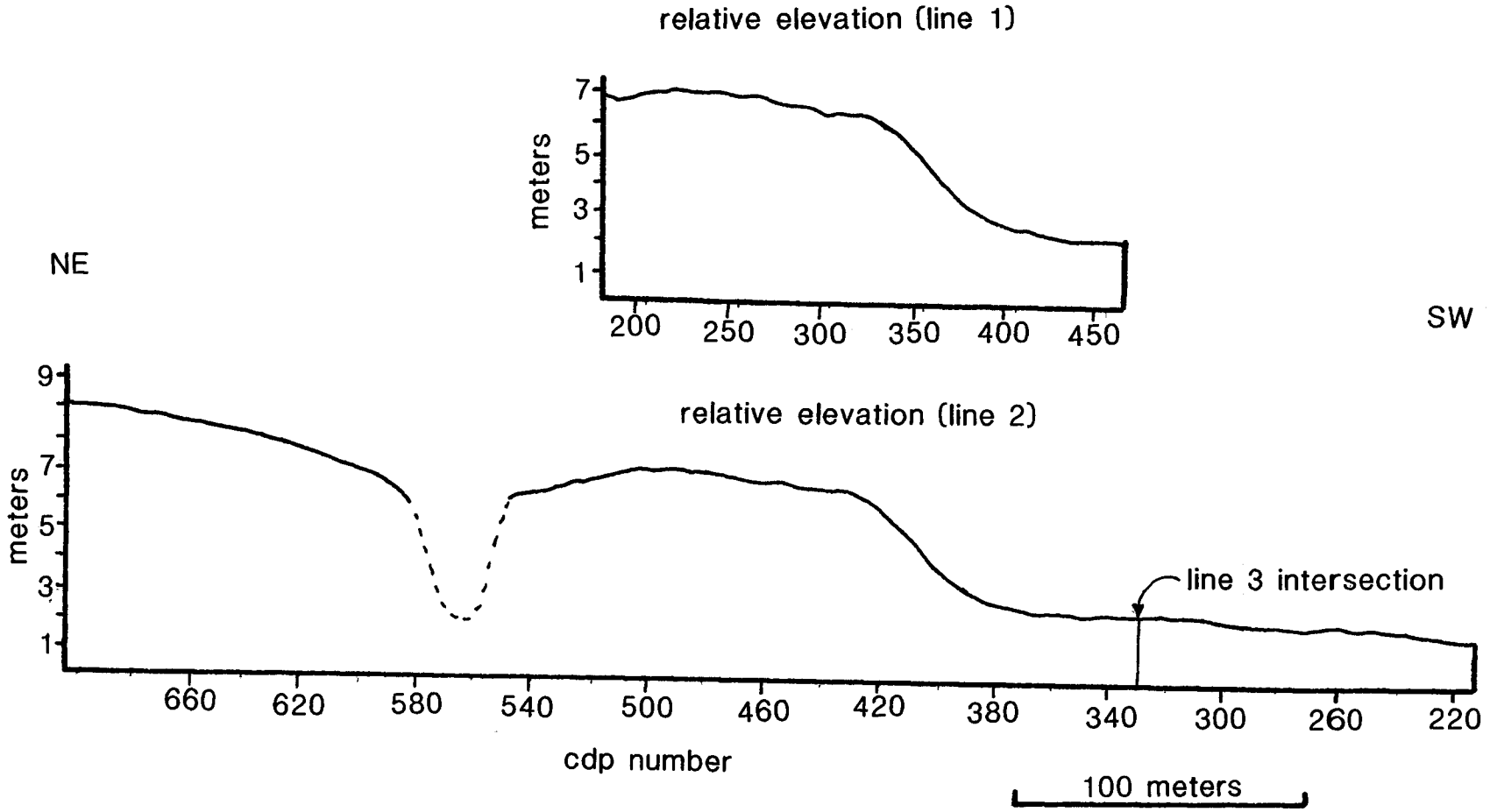
relative elevation (line 1)
meters
7
5
3
1
200
250
300
350
400
450
NE
SW
relative elevation (line 2)
meters
9
7
5
3
1
line 3 intersection
660
620
580
540
500
460
420
380
340
300
260
220
cdp number
100 meters

fairly consistent at approximately a 1 meter drop for every 40 meters toward the southwest. A stream channel located between CDP 545 and CDP 595 produced a significant change in elevation, making static corrections extremely difficult. The steepest portion of the fault scarp is located approximately between CDP 440 and CDP 370. This region correlates approximately to CDP 285 and CDP 310 respectively on line 1. The regional topographic slope mentioned above seems to dominate the remainder of both lines 1 and 2.

Relative elevation for line 3 changes by approximately 4 meters from the northeast to the southwest portion of the traverse (Figure 11). The topography is relatively consistent between CDP 190 and CDP 220. At CDP 220 the topography begins to ascend at a rate of approximately 1 meter for every 20 meters movement toward the southwest. At CDP 300 the topographic profile again flattens for the remainder of the traverse.

DATA PROCESSING

The majority of data processing was performed on a Data General MV-20000 mini-computer at the Kansas Geological Survey (KGS). The software used was the Seismic Processing Executive (SPEX) package by Sytech Inc. Additional programs written by Y. Chung, B. Bennett, and C.

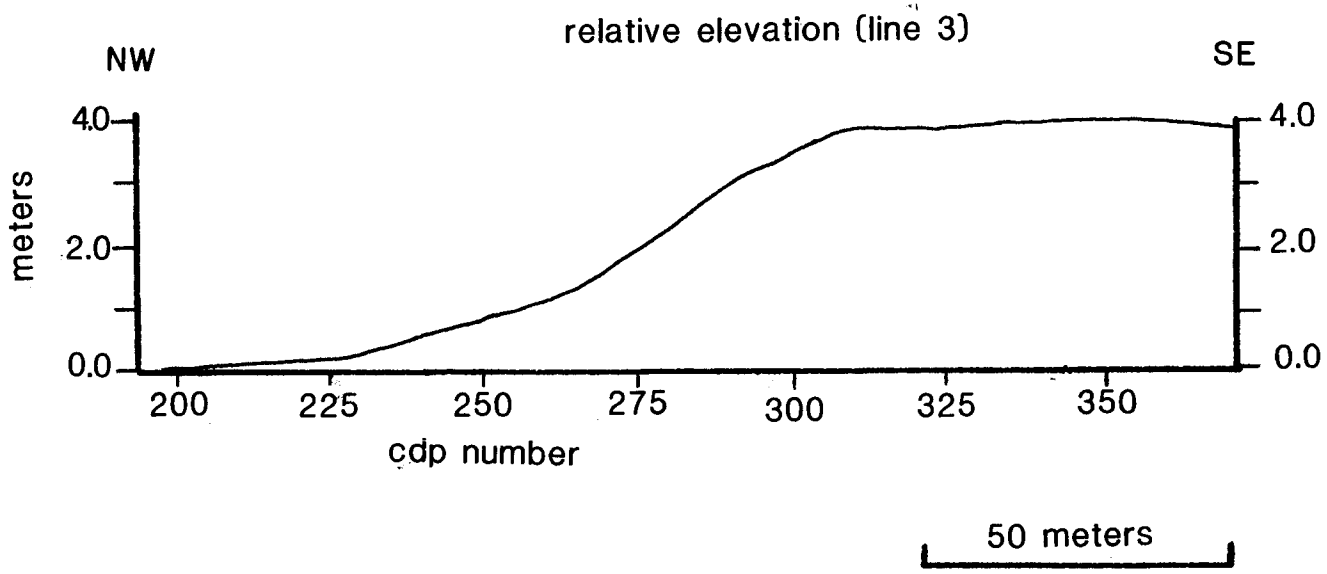

Figure 11. Relative elevation data for line 3. Elevation decreases by approximately 4 meters from the SE to the NW extents of line 3.

Somanas at the Kansas Geological Survey, and a Landmark RT Desktop Graphics Workstation were incorporated in the processing flow.

A similar processing flow was maintained for all three seismic lines. The processing flow included; converting raw field data to SEG-Y format in order to be compatible with the SPEX software, elevation (static) corrections, muting, editing, CDP sorting, velocity analysis, surface consistent statics, frequency spectral analysis, frequency filtering, and CDP stacking. In addition, an auto-predictive deconvolution filter was applied to line 2. Processing flow and parameters are summarized in APPENDIX: C.

Advanced processing techniques which included frequency-domain migration ($f-k$ migration) on line 1, and complex trace analysis with color plotting for all three lines were also performed. A more thorough discussion of complex trace analysis and $f-k$ migration are discussed in APPENDICES: D and E, respectively.

DISCUSSION

Detailed stratigraphic control in the study region is unavailable. This limits some of the interpretations. Total vertical displacement along the Meers Fault is speculated anywhere from one to a few kilometers.

Penetration of the seismic energy in this study is limited to depths of approximately 200 meters. Consequently, quantification of the vertical displacement along the fault is impossible. The discussion and interpretations related to vertical motion along the major fault associated with the scarp are limited to the orientation and relative motion of the structural blocks making up the shallow subsurface. Quantification of displacement along the major fault can be achieved with the drilling of two boreholes, one located on the northeast and one on the southwest flanks of the scarp. In addition to assumptions constraining interpretations of vertical motion, horizontal deformation is assumed to be predominantly a result of Post-Permian stress conditions. Maximum horizontal displacement during Holocene time is speculated at 25 meters (Ramelli and Slemmons, 1986). Any structure interpreted to be resulting from strike slip motion will therefore include displacement approximations.

Data quality of seismic line 1 remained good throughout the entire traverse of the fault. The three field records displayed in figure 12 are from the upthrown side (NE), directly over the scarp, and the downthrown (SW) portions of the fault respectively. All have high S/N and seismic reflections, refractions, and air-coupled waves that can be identified directly on the field files from all

Figure 12. Representative field files for line 1. The three files represent the upthrown NE (12a), directly over (12b), and downthrown SW (12c) portions of the scarp. Data for line 1 were collected with a 220 Hz low-cut (hi-pass) analog filter.

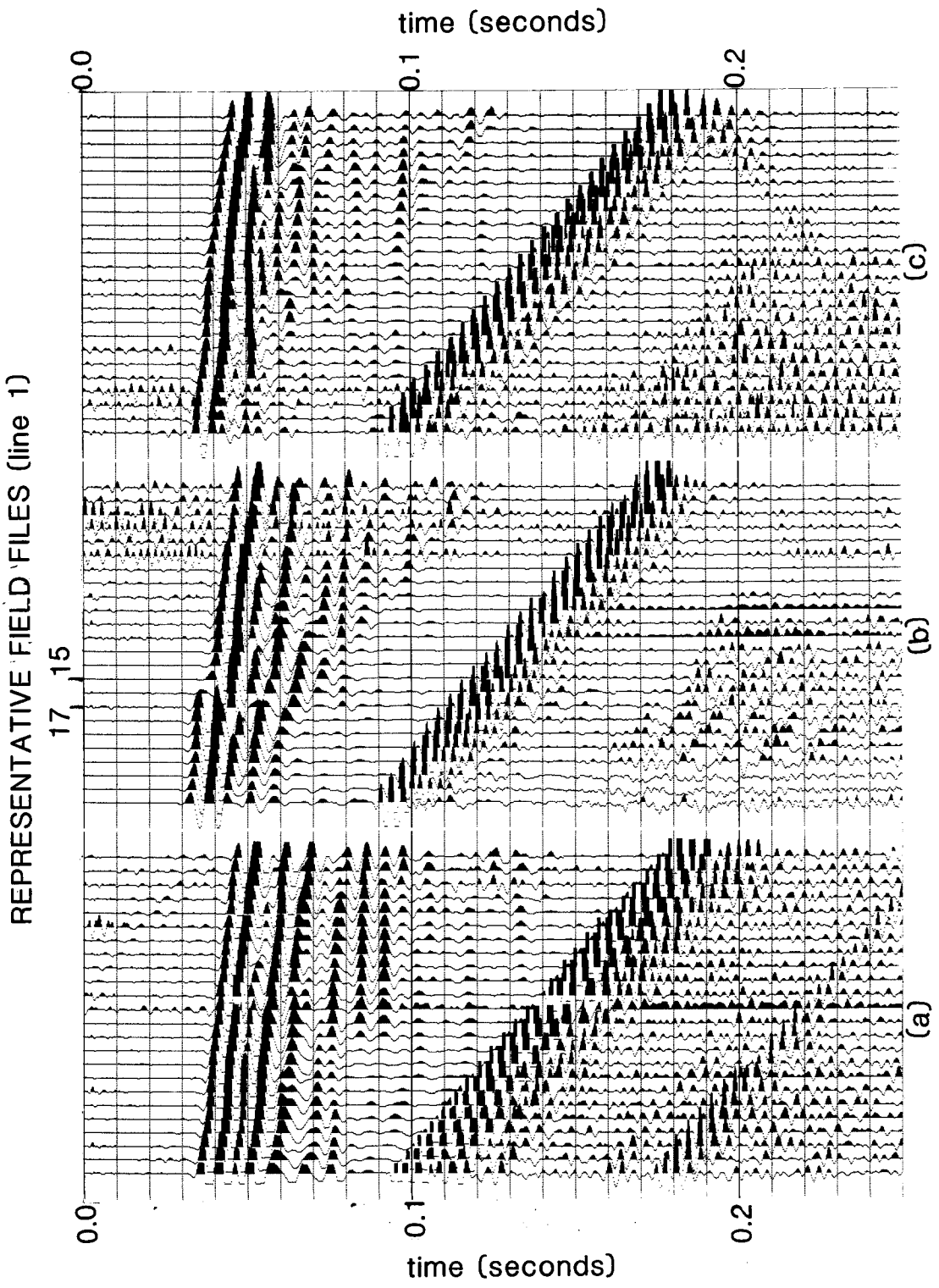
time (seconds)
0.0
0.1
0.2
(c)
(b)
(a)
REPRESENTATIVE FIELD FILES (line 1)
17
15
0.0
0.1
0.2
time (seconds)

three portions of the line. The surface waves arrived nearly simultaneously with the air-coupled waves. With the absence of identifiable reflection energy following the arrival of the air-coupled waves, the data were muted from the onset of the air-coupled waves to the end of the record. The first two arrivals on the field records (approximately 30 to 40 ms) are refractions and were muted during preliminary data processing. Most identifiable reflected energy arrives in a time window from approximately 50 to 120 ms possessing frequencies from 100 to 250 Hz.

Reflections from the upthrown (north) side of the fault scarp do not display the classical hyperbolic moveout (Figure 12a). Amplitude, frequency, and wavelet character changes as well as undulations in the arrival pattern of individually reflected events are indicative of structurally complex areas. The first reflected energy arrives at approximately 50 ms on the record. The divergence of this event from the refracted arrivals above allowed complete removal of refracted energy from the data without sacrificing the shallow reflector. All the coherent seismic energy arriving after the 50 ms reflector and before the air-coupled waves appears to be reflections.

The fault can be detected directly between traces labeled 15 and 17 on a record from over the fault zone

(Figure 12B). Similar to the upthrown side, the reflected energy first arrives at approximately 50 msec. The seismic energy does not appear to penetrate quite as deeply over the fault as on the flanks. This is probably due to the subsurface deformation within the fault zone. Orientation, frequency, and wavelet-character changes within individual reflectors again indicate deformational features along this portion of the line.

The reflected energy is significantly more coherent on the downthrown side of the fault scarp (Figure 12c). As on the upthrown side and directly over the scarp, most identifiable reflected energy arrives between approximately 50 and 120 ms. Seismic-energy penetration and S/N appear to vary from file to file on the downthrown side. This is primarily due to the relatively poor source-to-ground coupling when the source location was on or near the fault scarp.

To ensure correct identification of reflected events on the stacked section, all coherent arrivals observed on the field plots were visually inspected after each step of the processing flow. The shallowest two reflectors possess distinctively different characteristics than reflectors from deeper in the section (Figure 12). The angle of incidence of these reflectors is greater than the critical angle for each, making them wide-angle reflections. The

amplitude and frequency difference observed on these shallow wide-angle reflections can be attributed to either interference with the refracted arrivals, or wide angle caustic phenomena discussed by Pullan and Hunter (1985). These phenomena can most easily be seen on the far traces of the field plots.

The major faulting which produced the present day scarp can be seen in the subsurface between CDP 295 and CDP 315 (Figure 13) where coherency of reflected energy drops dramatically. The fault is oriented vertically to slightly dipping to the north with a relative up-to-the-north displacement.

The reduced amplitude of high frequency events that appear to be somewhat continuous across the fault can be attributed to horizontal oversampling (Figure 14). Horizontal oversampling results when the subsurface sampled points are closer than the diameter of a Fresnel zone. The radius (R) of the first Fresnel zone is $R \approx \sqrt{D\lambda/2}$, where D is the reflector depth, and λ is the reflected wavelength. The phenomenon seen here (increased frequency and decreased amplitude) results when part of the Fresnel zone around a particular subsurface sampling point begins to extend beyond the fault-related bed truncation. As more of the Fresnel zone passes beyond the bed truncation, the surface area available to reflect energy is reduced;

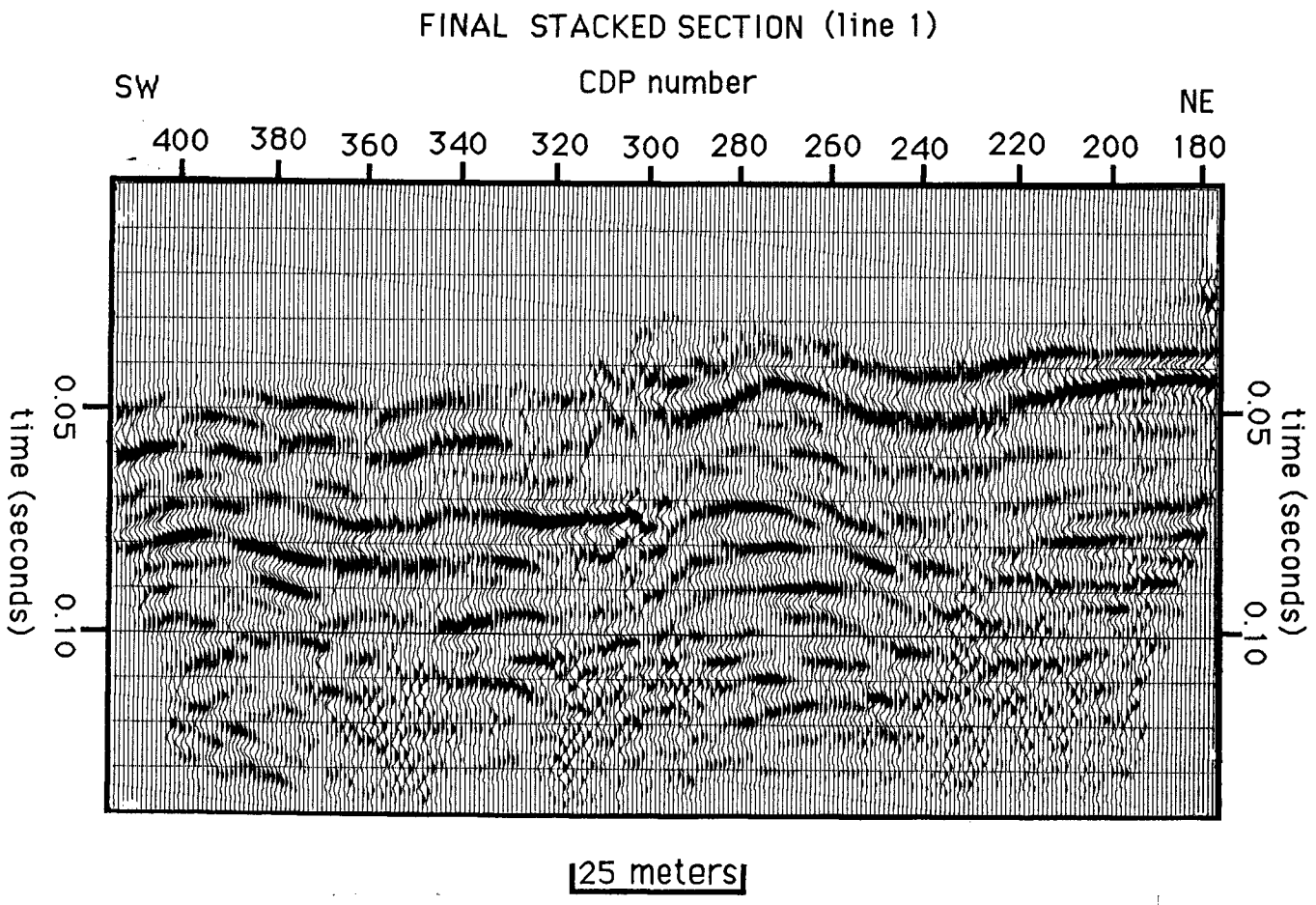

Figure 13. Final CDP stacked section for line 1. The fault associated with the scarp can be seen directly beneath CDP 300.

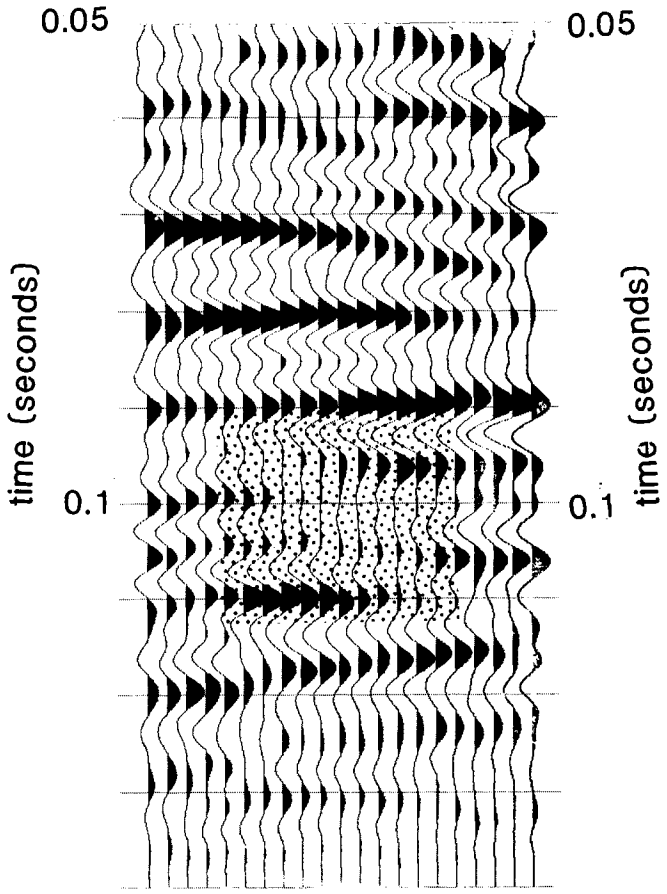

Figure 14. Horizontal oversampling phenomena results in decreased amplitude in conjunction with increased frequencies in the oversampled regions.

therefore, the amplitude of the returning energy is reduced. The decrease in effective Fresnel zone area in the case of bed truncation also causes the recorded frequency of the reflector to increase slightly. Since the Fresnel zone is large in comparison to the spacing of the subsurface sampling points, the reflector will appear to be thin and extend beyond the actual fault plane. This phenomenon resulting from horizontal oversampling was observed on all three seismic lines. Discussion of line 2 and 3 will refer to horizontal oversampling features without further mention of the nature in which the phenomena occur.

In addition to the major faulting which produced the scarp, there appears to be faulting on the upthrown (NE) and downthrown (SW) portions of the line. However, none of these faults are visible at the surface which suggests they have not been active for at least several thousand years. The upthrown portion of the line is characterized by both gentle folding and faulting deformation. Two parallel reverse slip faults appear to be dipping northward, transecting the seismic section at approximately CDP 268 and CDP 283, respectively. Coherent events appear to cross the faulted region. This is a result of the oversampling phenomenon discussed above. The downthrown (SW) portion of the line is characterized by significantly more coherent

reflected events. A reverse slip fault located at approximately CDP 384 appears to be dipping northward with a fault splaying off of it at approximately 80 to 100 ms and dipping to the south. There appears to be a fault running parallel to the northward dipping fault at CDP 384 approximately 20 m to the northeast. This fault is only evident at and below 85 ms. The horizontal oversampling remnants again are present in this faulted region.

Ability to interpret line 1 was enhanced with the addition of some complex trace analysis and color plotting. The complex trace attributes of instantaneous frequency and instantaneous phase were both calculated and observed. Both attributes appear to support what was observed on the real trace stacked CDP section.

Instantaneous frequency plots indicated a higher instantaneous frequency content in the faulted regions (Figure 15). The higher instantaneous frequencies are denoted by the darker blue and light purple colors. This observation results from the lower S/N caused by higher attenuation in the brecciated zone

The instantaneous phase information is the more beneficial complex trace attribute for this study. This is not surprising considering the properties of the instantaneous phase. Instantaneous phase, being completely independent from any amplitude information, emphasizes the

Figure 15. Instantaneous frequency section for line 1. Trends toward the higher instantaneous frequency values (blue) are associated with the faulted regions.

INSTANTANEOUS FREQUENCY (line 1)
SW
CDP number
NE
400 380 360 340 320 300 280 260 240 220 200 180
0.05
0.10
0.15
0.20
time (seconds)
25 meters

continuity of events. The faulted region associated with the scarp observed on the real seismic section between CDP 295 and CDP 315, can also be detected on the instantaneous phase section (Figure 16). The additional reverse-slip faulting observed on both the upthrown (NE) and downthrown (SW) portions of line 1 are also evident on the instantaneous phase section. Additional faulting located at CDP 360 appears possible based on the discontinuous nature of the events on the instantaneous phase section. The instantaneous phase display suggests the possibility of two intersecting reverse slip faults at approximately CDP 360. on the lowermost portion of the section (~130 ms down to 200 ms), the fault appears to dip to the north, whereas above ~130 ms the fault dips southward. Both intersecting faults appear to be reverse slip. The continuity of the event across this region at 60 ms suggests that the fault located at CDP 360 has been inactive since the deposition of the 60 ms reflector.

A composite interpretive line drawing based on the information given by each of the seismic sections is illustrated in figure 17. High angle reverse slip deformation dominates the interpretation, suggesting a compressional stress environment for the near-surface Meers Fault. The final interpretation can be derived from the real trace seismic section, and the instantaneous phase

Figure 16. Instantaneous phase section for line 1. Discontinuities observed on the instantaneous phase section were crucial to the emplacement of interpreted faulting.

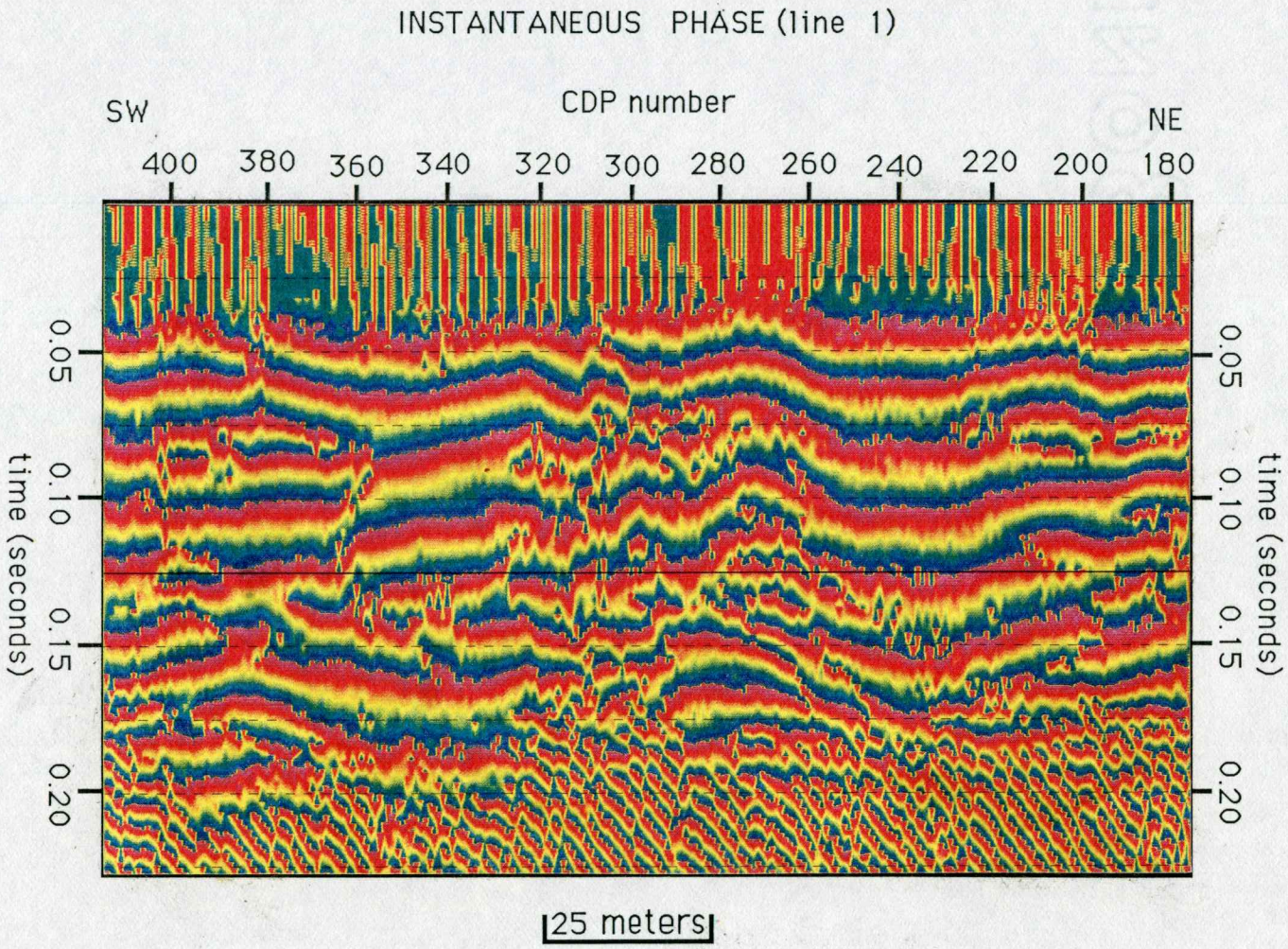
INSTANTANEOUS PHASE (line 1)
SW
CDP number
NE
400
380
360
340
320
300
280
260
240
220
200
180
0.05
0.10
0.15
0.20
time (seconds)
25 meters

Figure 17. Interpretive line drawing for line 1. derived from both the real trace and complex trace sections.

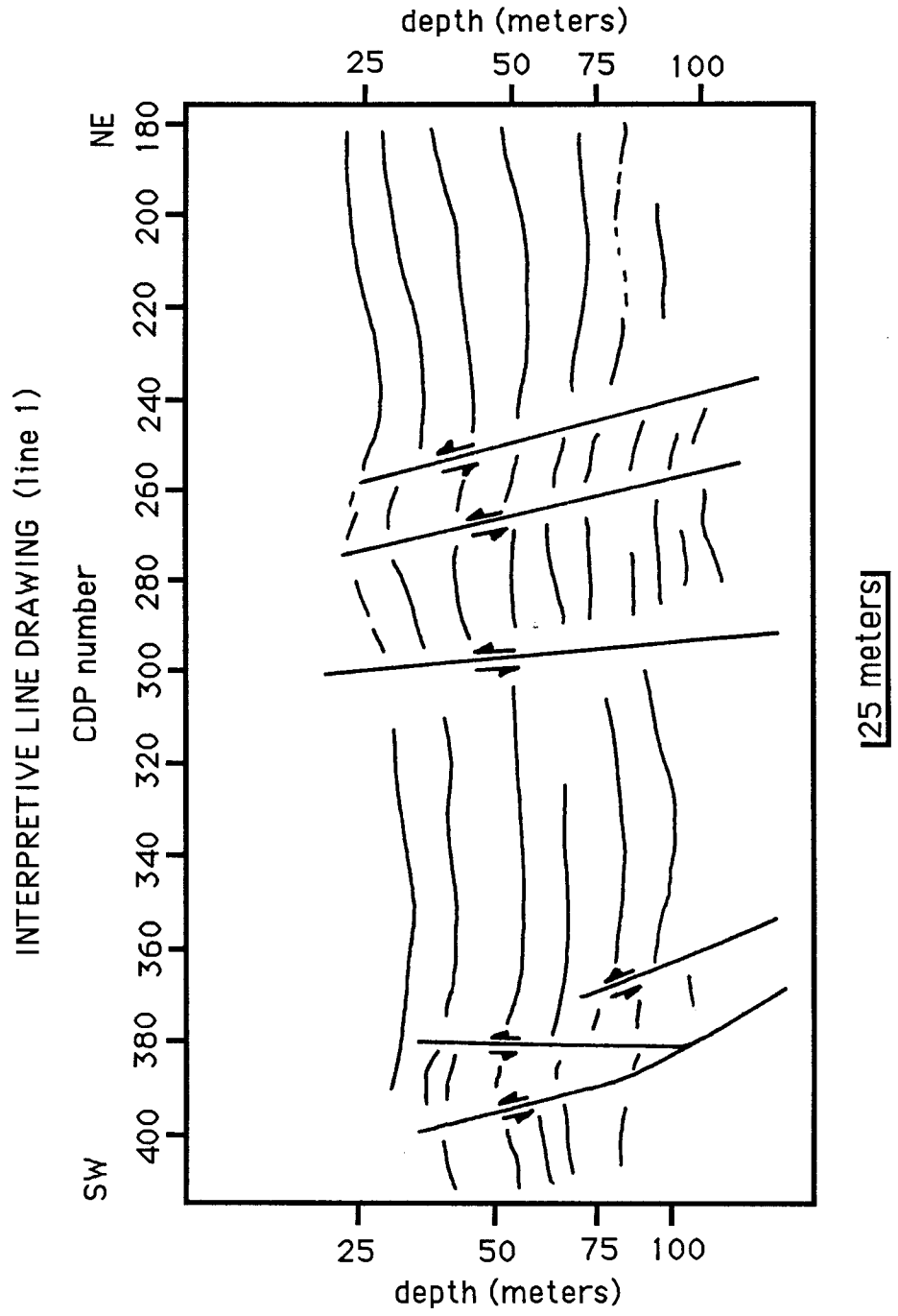
INTERPRETIVE LINE DRAWING (line 1)
depth (meters)
25
50
75
100
NE
SW
CDP number
180
200
220
240
260
280
300
320
340
360
380
400
25 meters

section individually. However, combining information from all three sources results in a composite interpretation which holds significantly more validity.

Depth scales displayed on the interpretation are based on stacking velocities that range from 1300 m/s to 1830 m/s. Velocity analysis was extremely difficult due to the minimal horizontal sampling distance for each field record. Reflection information visually stacked is nearly the same for a range of velocities making the exact velocity essentially impossible to determine. Therefore, the depth scales are only approximations.

Data quality of seismic line 2 had a slightly lower S/N due to an increase in wind noise. The three field records displayed in figure (18) are examples of relatively better data quality files from the upthrown (NE), directly over the scarp, and the downthrown (SW) portions of the fault respectively. Although the S/N ratio was slightly lower than that for line 1, the seismic reflections, refractions, and the air-coupled wave can be identified on all three portions of the line. Surface wave energy arrives after the air-coupled wave. Reflection energy is not identifiable later than the air-coupled wave arrival, however the air-coupled wave was surgically removed leaving the data arriving later in time. Most identifiable reflection energy arrives in a time window from

Figure 18. Representative field files for line 2. The three files represent the upthrown NE (18a), directly over (18b), and the downthrown SW (18c) portions of the scarp. Data for line 2 were recorded with a 110 Hz low-cut (hi-pass) analog filter.

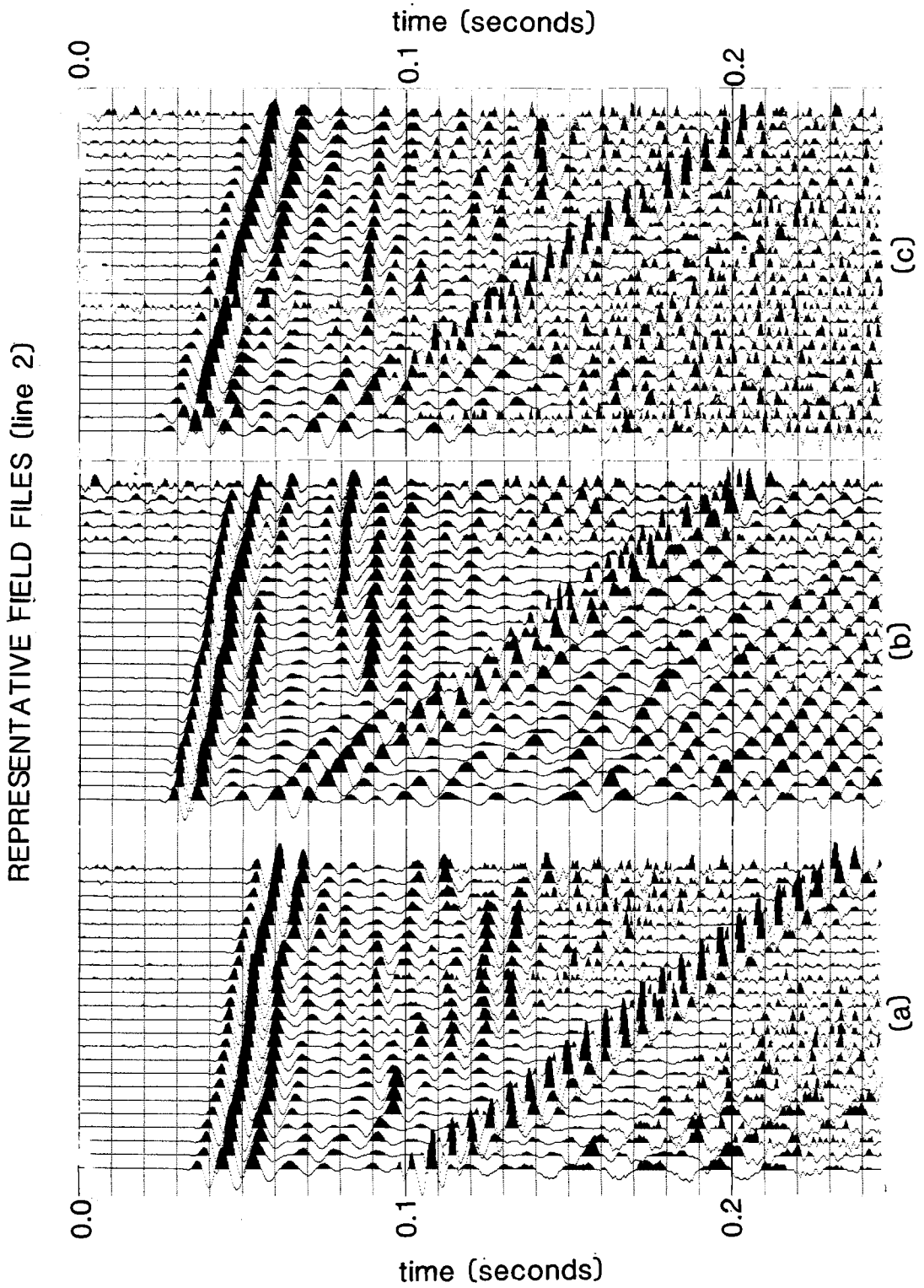
REPRESENTATIVE FIELD FILES (line 2)
time (seconds)
0.0
0.1
0.2
(c)
(b)
(a)
0.0
0.1
0.2
time (seconds)

approximately 40 ms to 150 ms. Energy penetration seems to be slightly deeper than for line 1. This is related to the method of shothole drilling. Shotholes from line 1 were augered using a hand held auger that often resulted in less than adequate shotholes. As a result, source-to-ground coupling was significantly less than desired for several shots. Shotholes for line 2 and 3 were augered using a trailer-mounted auger which resulted in near perfect shotholes for every station. This resulted in significantly better source-to-ground coupling and hence deeper energy penetration. Dominant frequencies range approximately from 90 to 150 Hz, a much lower range than frequencies for line 1. Lower dominant frequencies can be attributed to use of 110 Hz rather than 220 Hz analog filters used recording.

The representative field record from the upthrown portion of the fault (Figure 18a) is from approximately 100 meters farther northeast than the representative field record for line 1. In contrast to the record from line 1, the record displays reflected events which illustrate the classical hyperbolic moveout. Amplitude and frequency characteristics for the reflected arrivals seem reasonably consistent suggesting that seismic line 2 may extend northeastward beyond the deformed units associated with the faulting The refracted energy appears to ring for

approximately 30 ms interfering with the first reflected arrival. Evidence for divergence of the third event at approximately 50 ms on several field files implies the first arrival of reflected energy. Due to the apparent ring of the refraction, separation of the refracted energy from the reflected energy is significantly more difficult for line 2 and therefore first-arrival muting of the refractions was neglected. The 50 ms reflection was therefore carefully monitored through the processing flow to the final stacked section. Any energy prior to this event was considered refraction energy and was ignored.

Similar to line 1, the field records directly over the scarp display more complexity in the reflected arrivals (Figure 18b). Orientation, frequency, amplitude, and wavelet character changes within individual reflected events indicate significant deformation. Reflected energy appears to arrive in the 40 to 50 ms range. Detection of the fault associated with the scarp is not as obvious as on the records over the scarp on line 1. This is probably due to the decrease in S/N.

Reflection energy on the downthrown (SW) portion of the scarp is fairly coherent for line 2 and resembles the data observed on the downthrown portions of line 1 (Figure 18c). Wind noise posed a much greater problem on this portion of the survey. Wind gusts increased in the late

afternoon during the time these data were acquired. The representative field record from the downthrown (SW) portion nicely illustrates the drop in S/N due to the wind noise.

The major faulting that produced the present day scarp along with the additional faulting observed on line 1 is obvious on the line 2 stacked seismic section (Figure 19). The major fault which produced the scarp can be seen in the subsurface between CDP 440 and CDP 450. Data quality reduces dramatically in this area. The two parallel northward dipping faults observed on line 1 can be located at CDP 480 and CDP 490 respectively. The northward dipping fault and its southward dipping splay observed on the downthrown portion of line 1 is evident in the subsurface between CDP 360 and CDP 395. The last fault noticed on line 1 (approximately 20 m north of the splayed fault on the downthrown portion) can be seen in the subsurface between CDP 425 and CDP 430.

The two areas of missing data on the northeastward side of the stacked section are due to the presence of a stream channel. Unsuccessful attempts were made to fire the source while recording on the opposite side of the stream providing coverage under the stream channel. The channel transects the seismic survey between CDP 545 and CDP 595. The majority of the data under the stream were of

Figure 19. Final CDP stacked section for line 2. The fault associated with the scarp can be seen directly beneath CDP 450.

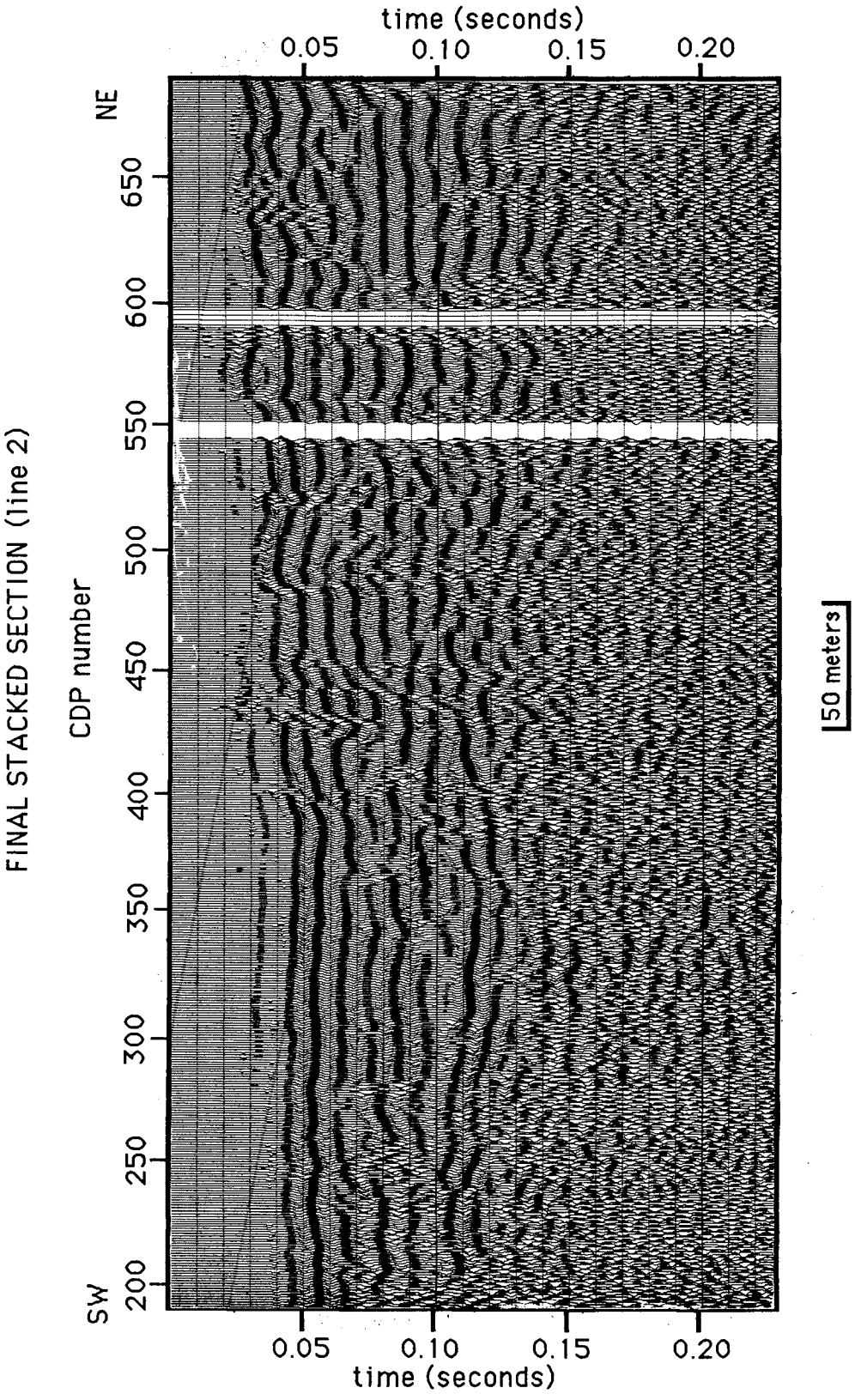
FINAL STACKED SECTION (line 2)
time (seconds)
0.05
0.10
0.15
0.20
NE
650
600
550
500
450
400
350
300
250
200
SW
CDP number
50 meters
0.05
0.10
0.15
0.20
time (seconds)

good quality, but the fold and quality at both the northeast and southwest banks of the stream channel decreased considerably. The decrease in fold and quality resulted in gaps in the section between CDP 545 and CDP 550 and also between CDP 590 and CDP 595. Data from within the edges of the stream channel possessed a bulk static delay in arrival of the reflected events of approximately 17 ms. Therefore, a bulk static shift up in time was applied to return this portion of the data back to where it correlated with each side of the stream channel. It is possible, but not likely, that part of this shift could be caused by a graben that exactly coincides with the stream channel location. This is doubtful, however, because there are no signs of diffractions or other unusual disturbances in this part of the seismic section.

The only significant structure observed on the upthrown (NE) portion of the line, beyond what was observed on line 1, occurs on the north side of the stream channel. A northward dipping fault can be observed in the subsurface between CDP 640 and CDP 650. Displacement along the fault only occurs below 100 ms. A coherent reflection at 90 ms covers the faulted area suggesting inactivity since the deposition of the 90 ms reflecting unit. Otherwise, data from the stream northward are relatively undisturbed

suggesting that the deformation is concentrated south of the stream channel.

Extending line 2 to the southwest beyond the southern extent of line 1 resulted in exposure of additional deformation to the southwest. The geologic units appear to be undisturbed for 80 meters between CDP 280 and CDP 360. A northward dipping fault can be observed in the subsurface between CDP 275 and CDP 280. Movement along this fault seems to be minimal, no more than 4 ms. In addition, a northward dipping fault and an associated vertical splay can be seen between CDP 230 and CDP 260.

The horizontal oversampling phenomenon observed and discussed in detail for line 1 is also present in line 2. The reduced amplitude of these high frequency events gives the appearance of continuous reflectors across the faulted regions.

Complex trace analysis and color plotting provided an additional source from which to draw subsurface information. Instantaneous phase and instantaneous frequency analysis added a different perspective and substantiated what was observed on the real-trace stacked seismic section.

The instantaneous phase (Figure 20) information provided a detailed picture of the continuity of events and was a major contribution to the interpretation of the

Figure 20. Instantaneous phase section for line 2. Discontinuities on the phase section helped to emphasize what was observed on the real trace section.

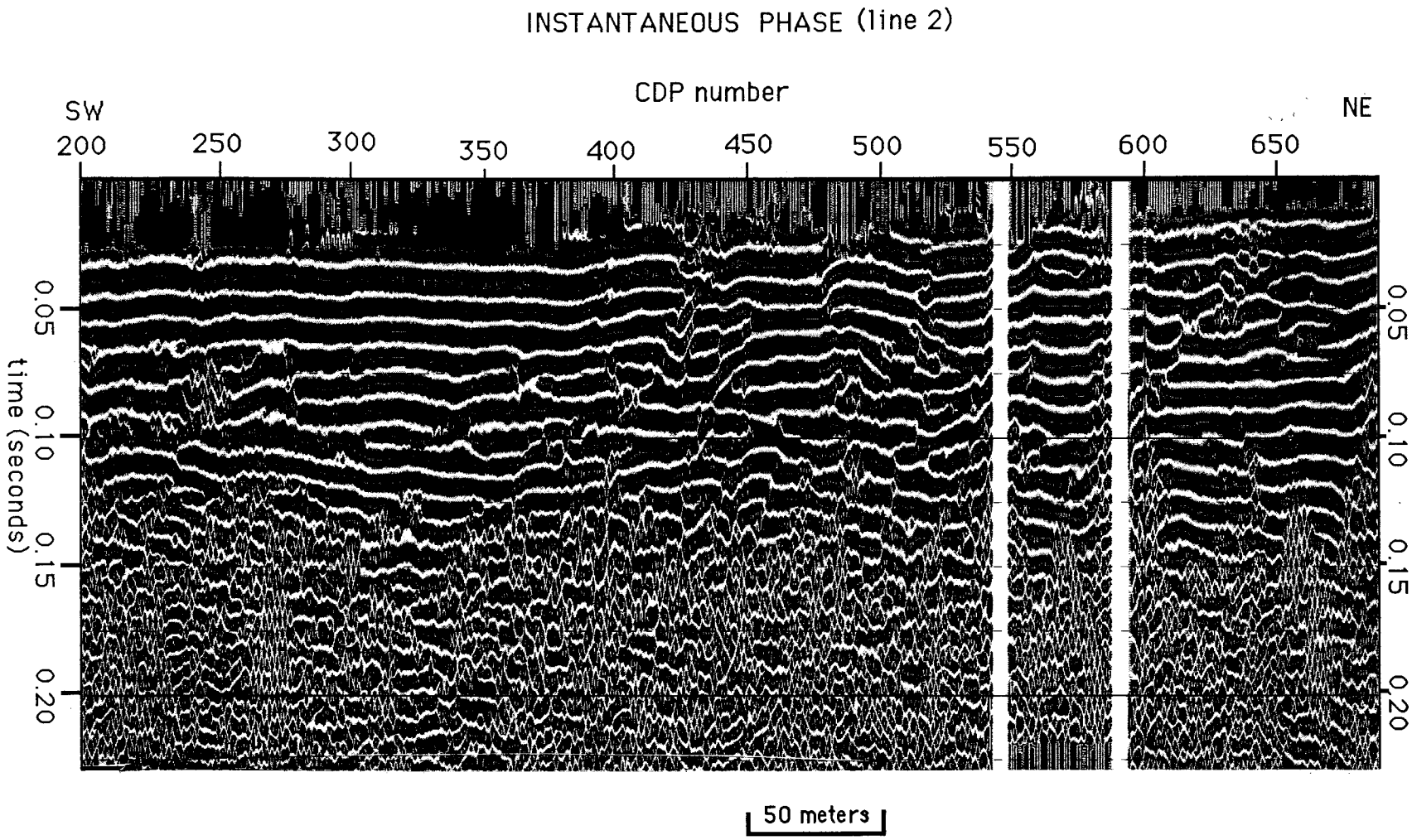
INSTANTANEOUS PHASE (line 2)
CDP number
SW
NE
200
250
300
350
400
450
500
550
600
650
0.05
0.10
0.15
0.20
time (seconds)
50 meters

orientation and sense of motion on each of the faults observed in the real-trace-seismic section. Color-coding for the instantaneous phase section was the same as that used for line 1.

The instantaneous frequency (Figure 21) plot in itself did not provide any additional information. However, there appears to be an increase in the frequencies in the faulted regions. This phenomenon lends support to the placements of the faults.

The interpretive line drawing (Figure 22) is primarily derived from the real-trace stacked seismic section and the instantaneous phase section. Recognition of the same features on both the real-trace section and the instantaneous phase section gives the interpretation significantly more validity. Relatively higher amplitude events are sketched in the line drawing. Correlating these units across the major fault zone which produced the present-day scarp would be speculative without detailed stratigraphic information. Correlation across the rest of the faulting seems reasonable because displacement across these faults appears to be minimal, possibly no more than 5 to 10 meters.

Depth scales displayed on the sides of the interpretation are based on stacking velocities that range from 1200 m/s to 2000 m/s. Similarly to line 1, reflected

Figure 21. Instantaneous frequency section for line 2.

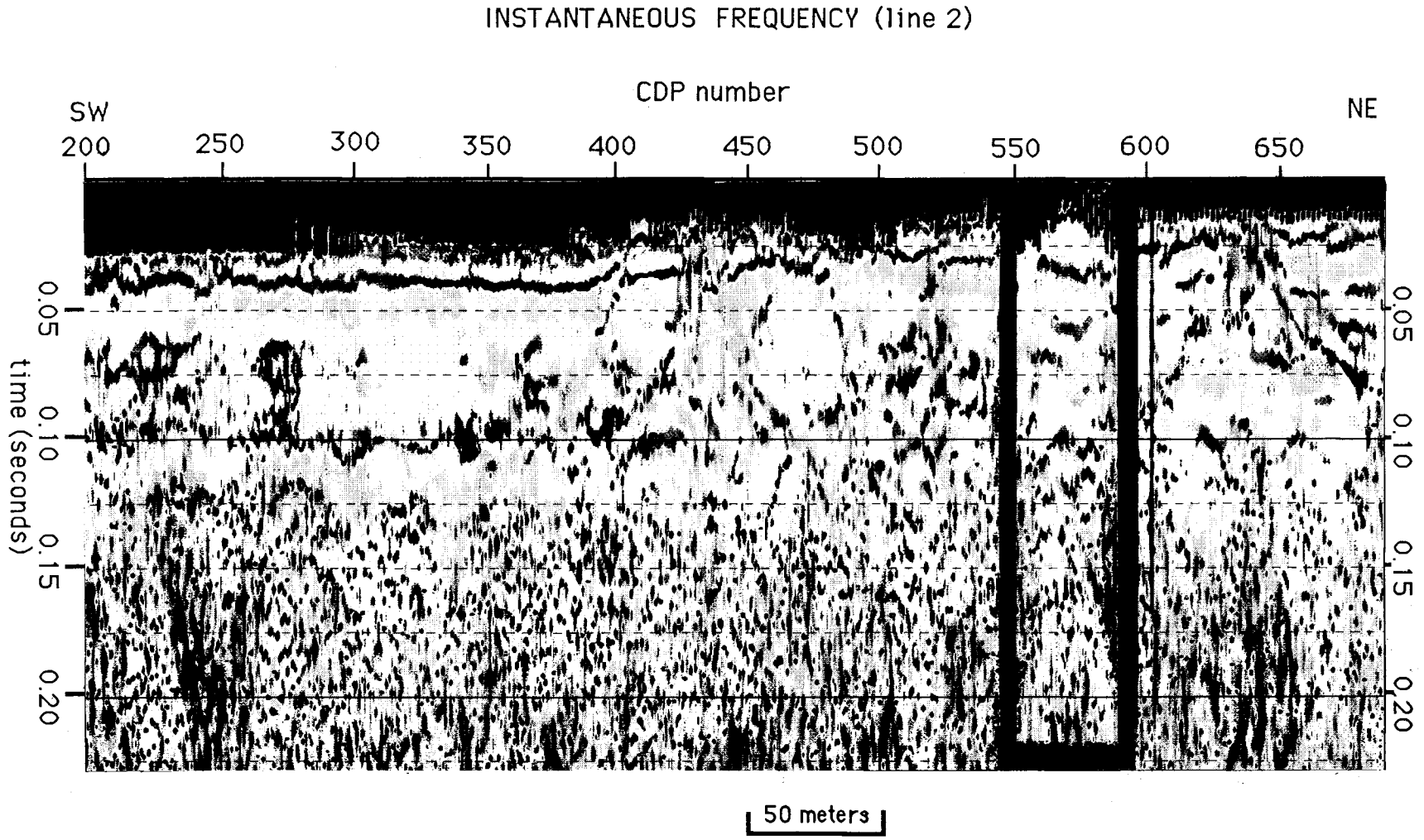
INSTANTANEOUS FREQUENCY (line 2)
CDP number
SW
NE
200
250
300
350
400
450
500
550
600
650
time (seconds)
0.05
0.10
0.15
0.20
50 meters

Figure 22. Interpretive line drawing for seismic line 2 derived from both the real trace and complex trace sections.

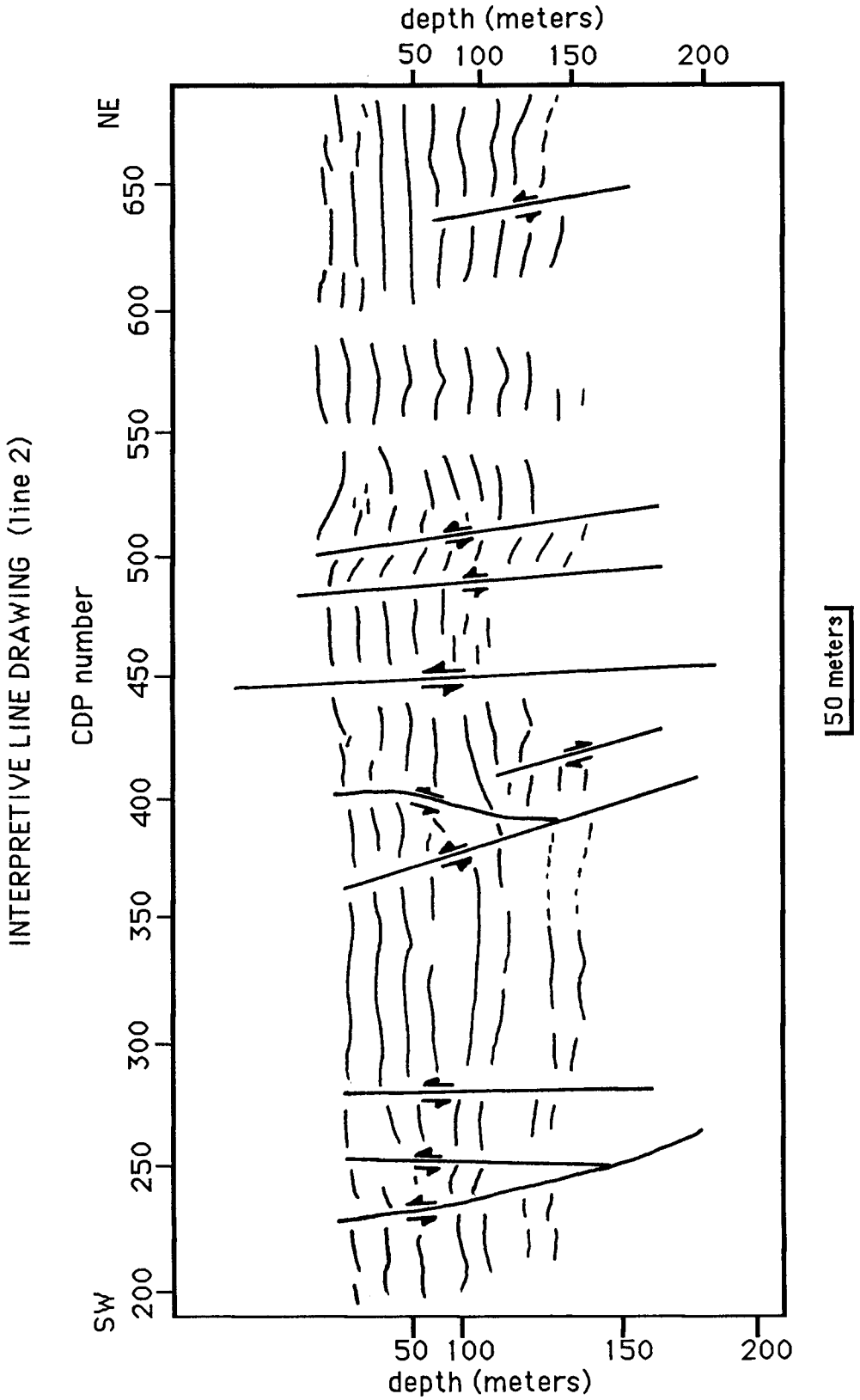
INTERPRETIVE LINE DRAWING (line 2)
depth (meters)
50 100 150 200
NE
650
600
550
500
450
400
350
300
250
200
SW
CDP number
50 meters
50 100 150 200
depth (meters)

energy visually stacked in at a range of velocities. Therefore, choosing the exact velocity was impossible. Consequently, the depth scales are only approximations.

Data on line 3 possess a S/N comparable to that of line 1 and 2. Dominant frequencies appear to be slightly lower than in line 1 probably due to the different analog low-cut filtering. Figure (23) represents typical field records on the northwest and southeast sides of the CDP traverse respectively. Seismic reflections, refractions, and the air-coupled wave can be identified directly on the field plots. A second zero-crossing first arrival mute helped to remove most of the refracted energy. The refracted energy that remained was carefully monitored throughout the processing and interpretation stages to ensure no refraction energy was misidentified as reflections. Dominant frequencies of the reflected energy range from approximately 100 to 150 Hz. Reflection energy observed on the field files appear to be disturbed along portions of the line. Energy penetration seems consistent from file to file.

Reflected energy observed on the field files was monitored throughout the processing flow to the final stacked section (Figure 24). Normal dip slip faulting appears to prevail throughout line 3 suggesting an extensional stress field associated with the lateral

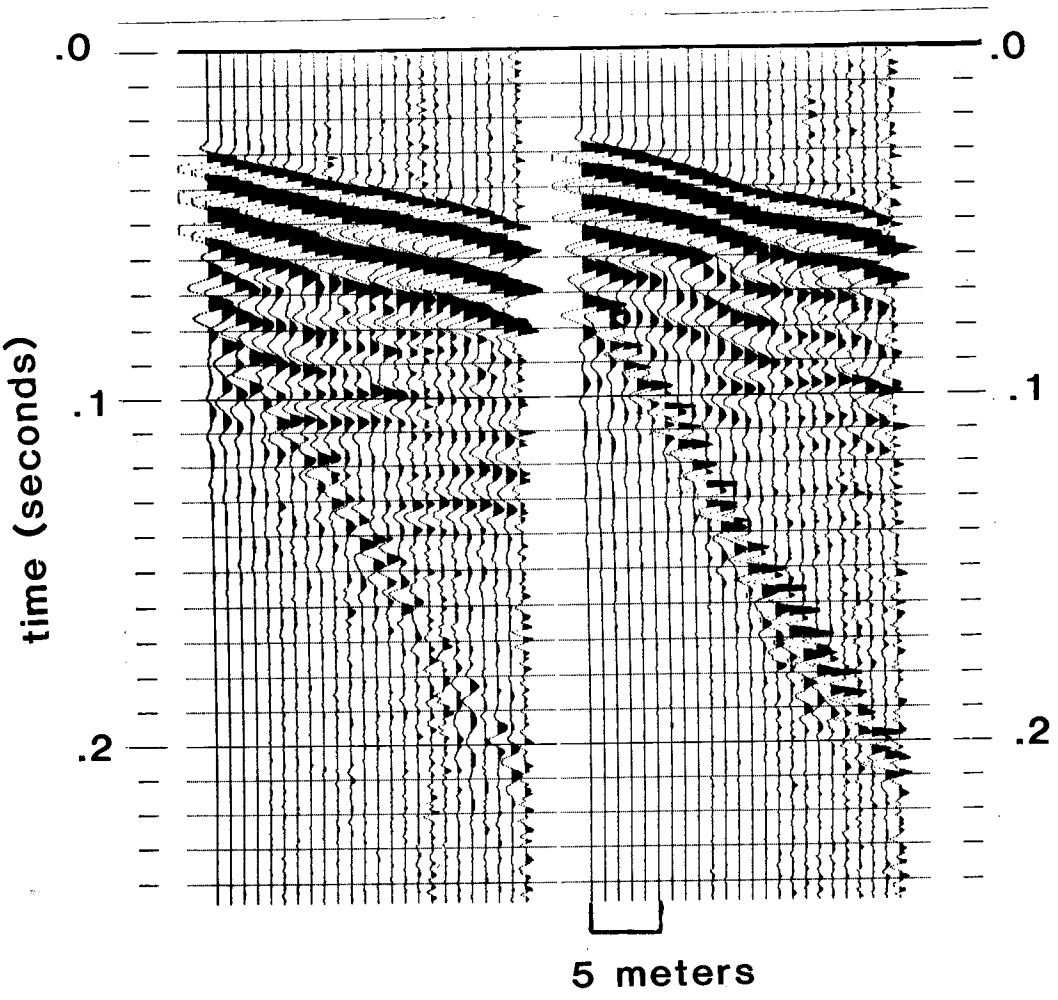

Figure 23. Representative field files for line 3. The two files represent the NW and SE portions of the line respectively. Data for line 3 were collected with a 110 Hz low-cut (hi-pass) analog filter.

Figure 24. Final CDP stacked section for line 3. The major feature is a graben located between CDP 260 and 300.

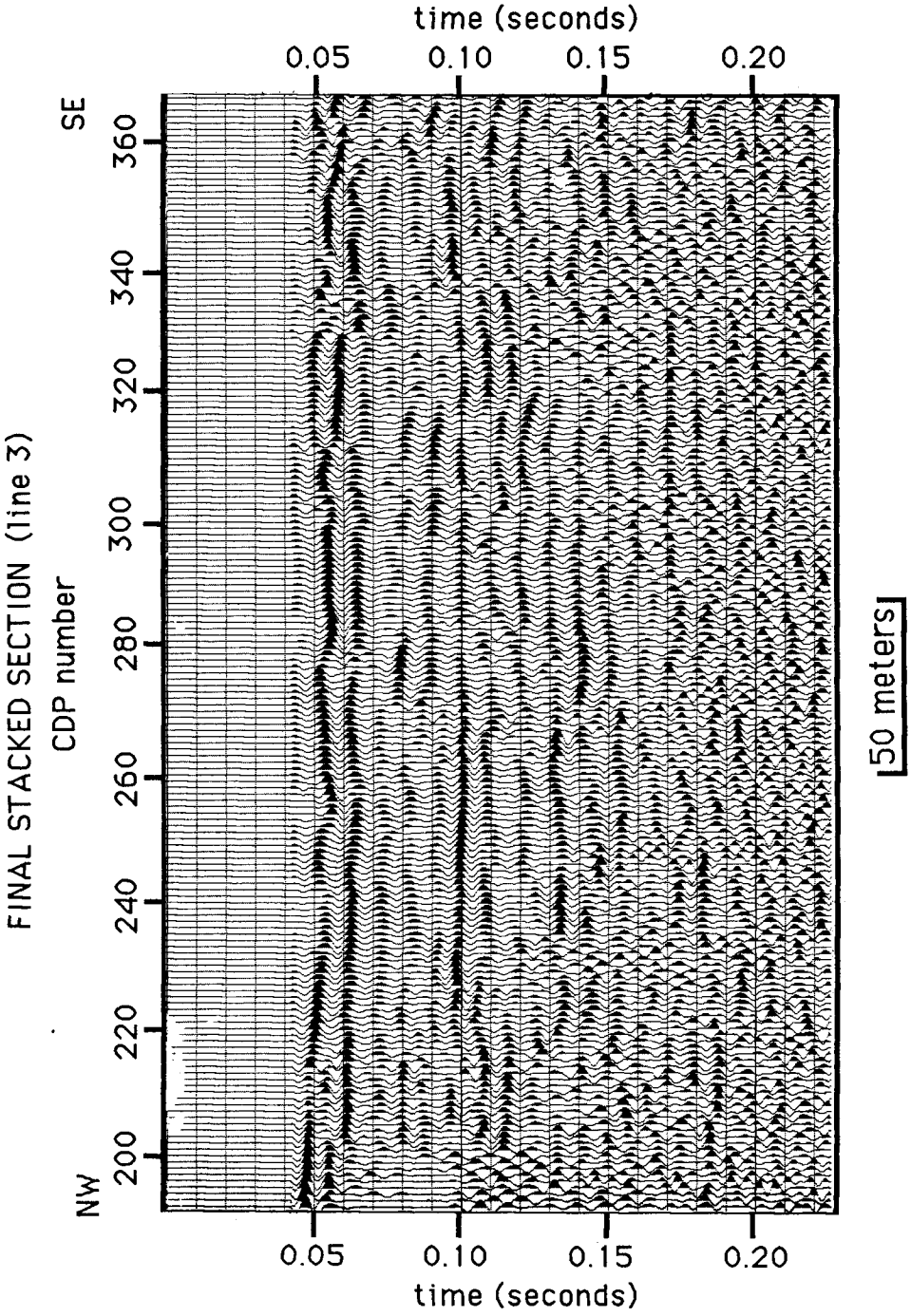
time (seconds)
0.05
0.10
0.15
0.20
SE
360
340
320
300
280
260
240
220
200
NW
FINAL STACKED SECTION (line 3)
CDP number
50 meters
0.05
0.10
0.15
0.20
time (seconds)

movement along this small sample of the fault zone. Discontinuities of events observed on the instantaneous phase data support the faulting seen on the real-trace stacked section (Figure 25). In addition, the instantaneous frequency (Figure 26) in itself is non-conclusive but supports the results observed in the other sections. Anomalous high frequency energy appears to be concentrated in the faulted regions as observed with both line 1 and line 2.

The primary geologic feature on line 3 is a graben located between CDP 265 and CDP 300. Displacement in the graben is extremely difficult to quantify due to the lack of stratigraphic and velocity control. Figure 27 displays a CDP section of line 3 stacked using a constant velocity of 1250 m/s and the same section illustrating the graben with a 10 ms (6.2m) displacement. Figure 28 displays a CDP section of line 3 stacked using a constant velocity of 2000 m/s and the same section with a 31 ms (31m) displacement in the graben. Figures 27 and 28 illustrate the importance of velocity control in making the correct interpretation of displacement. A conservative estimation of displacement in the graben is approximately 5 to 30 meters. In addition to the graben, there appears to be minor normal faulting located at approximately CDP 210, 320, 350, and 360, respectively. Movement does not appear to be quite as

Figure 25. Instantaneous phase section for line 3. Discontinuities observed on the phase section support what was observed on the real trace section.

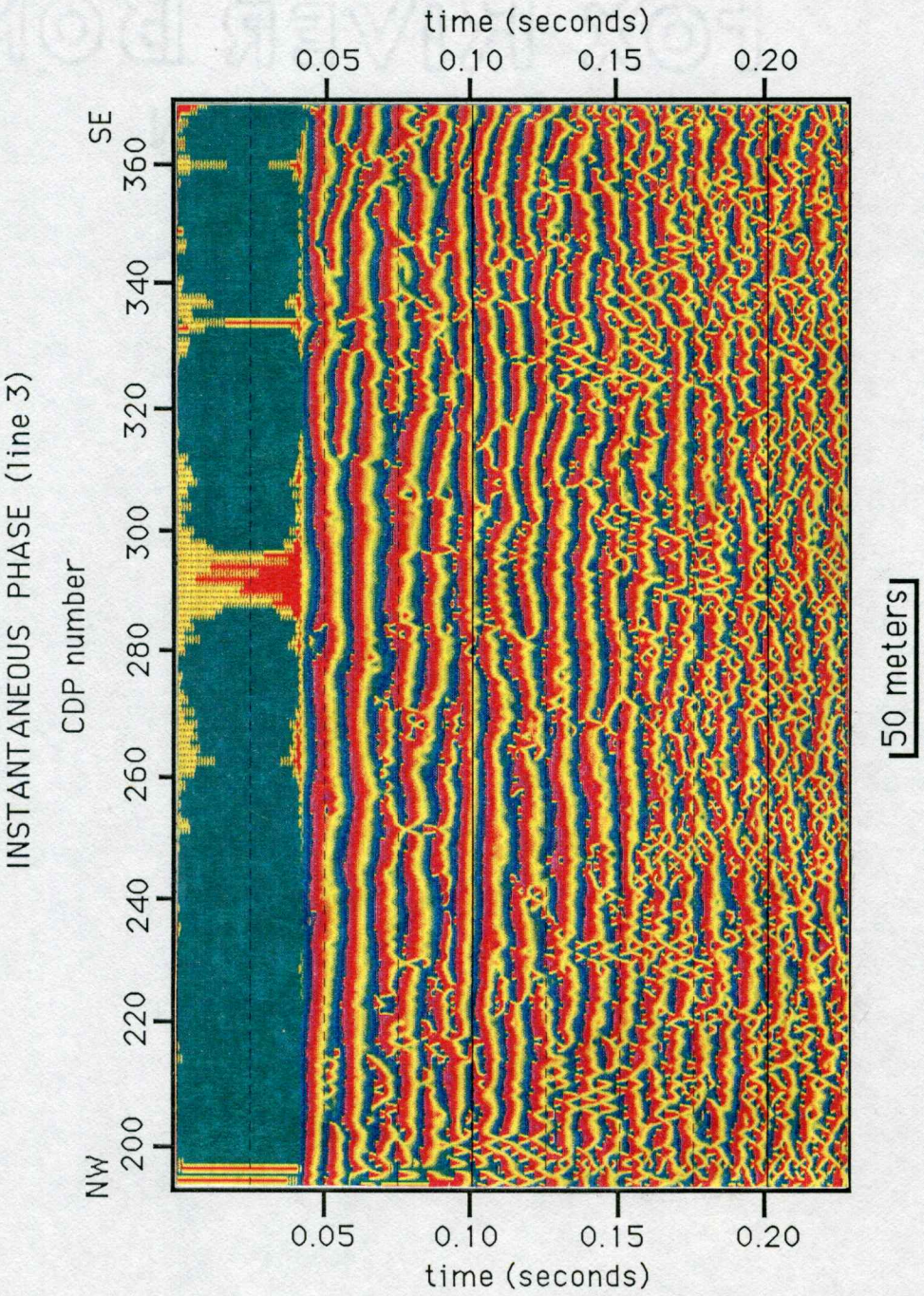
INSTANTANEOUS PHASE (line 3)
time (seconds)
0.05
0.10
0.15
0.20
CDP number
NW
200
220
240
260
280
300
320
340
360
SE
50 meters

Figure 26. Instantaneous frequency section for line 3. Higher instantaneous frequency values (blue) appear in the faulted regions of the line.

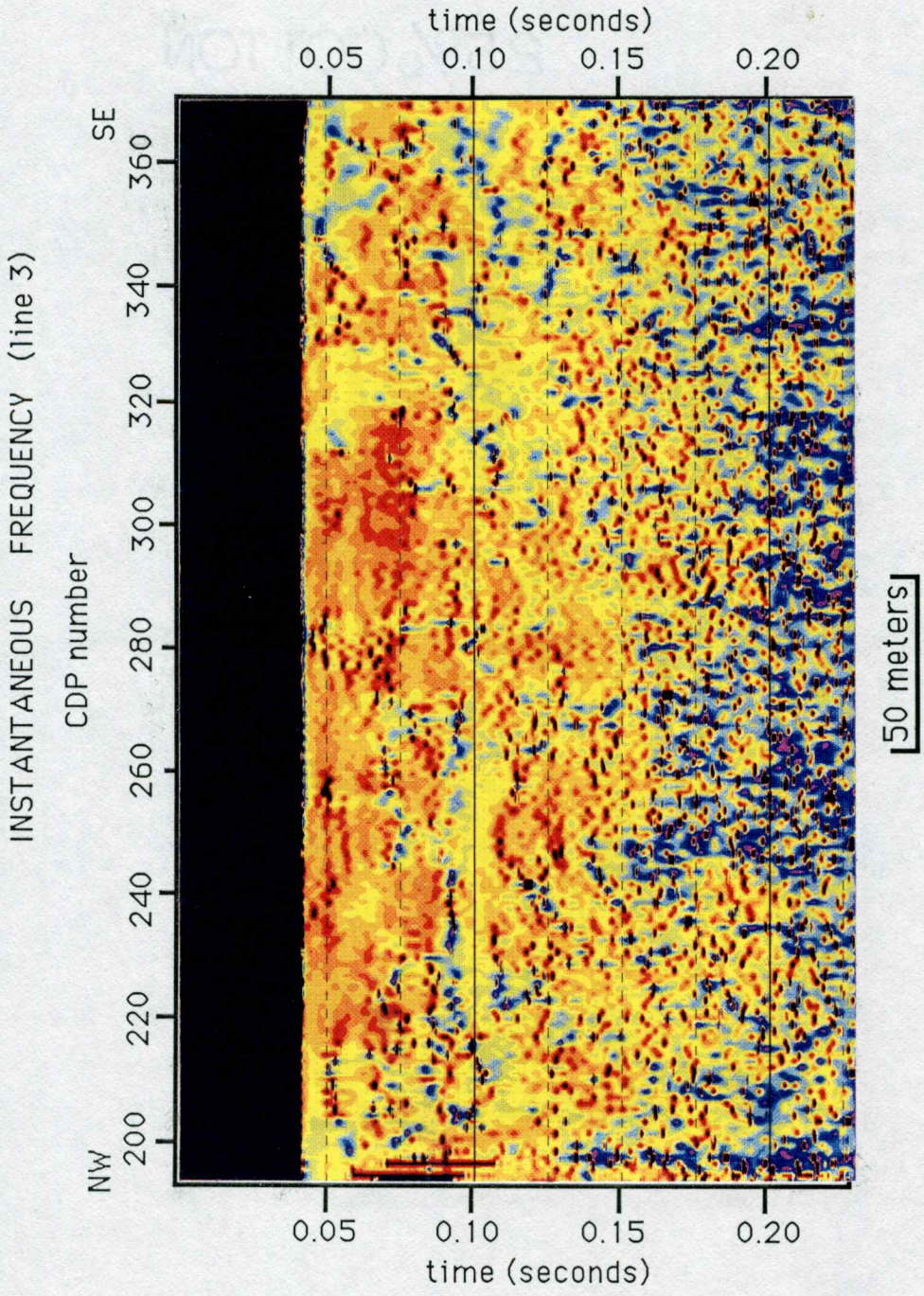
time (seconds)
0.05
0.10
0.15
0.20
SE
360
340
320
300
280
260
240
220
200
NW
CDP number
INSTANTANEOUS FREQUENCY (line 3)
50 meters
0.05
0.10
0.15
0.20
time (seconds)

Figure 27. Brute stack of line 3 with a constant velocity of 1250 m/s resulting in an interpreted displacement on the graben of approximately 6.2 meters.

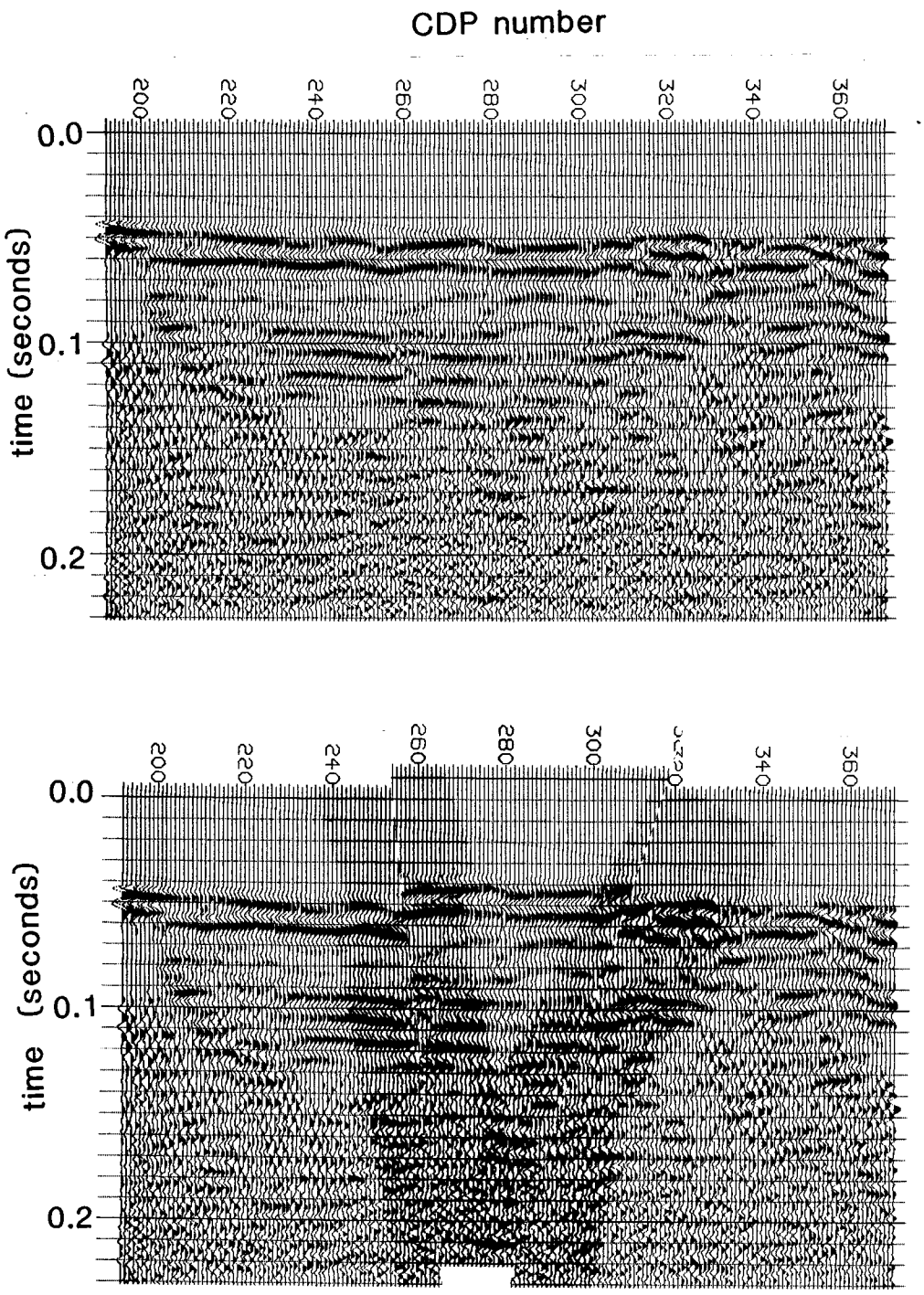
CDP number
200
220
240
260
280
300
320
340
360
0.0
0.1
0.2
time (seconds)
200
220
240
260
280
300
340
360
0.0
0.1
0.2
time (seconds)

Figure 28. Brute stack of line 3 with a constant velocity of 2000 m/s resulting in an interpreted displacement in the graben of approximately 31 meters.

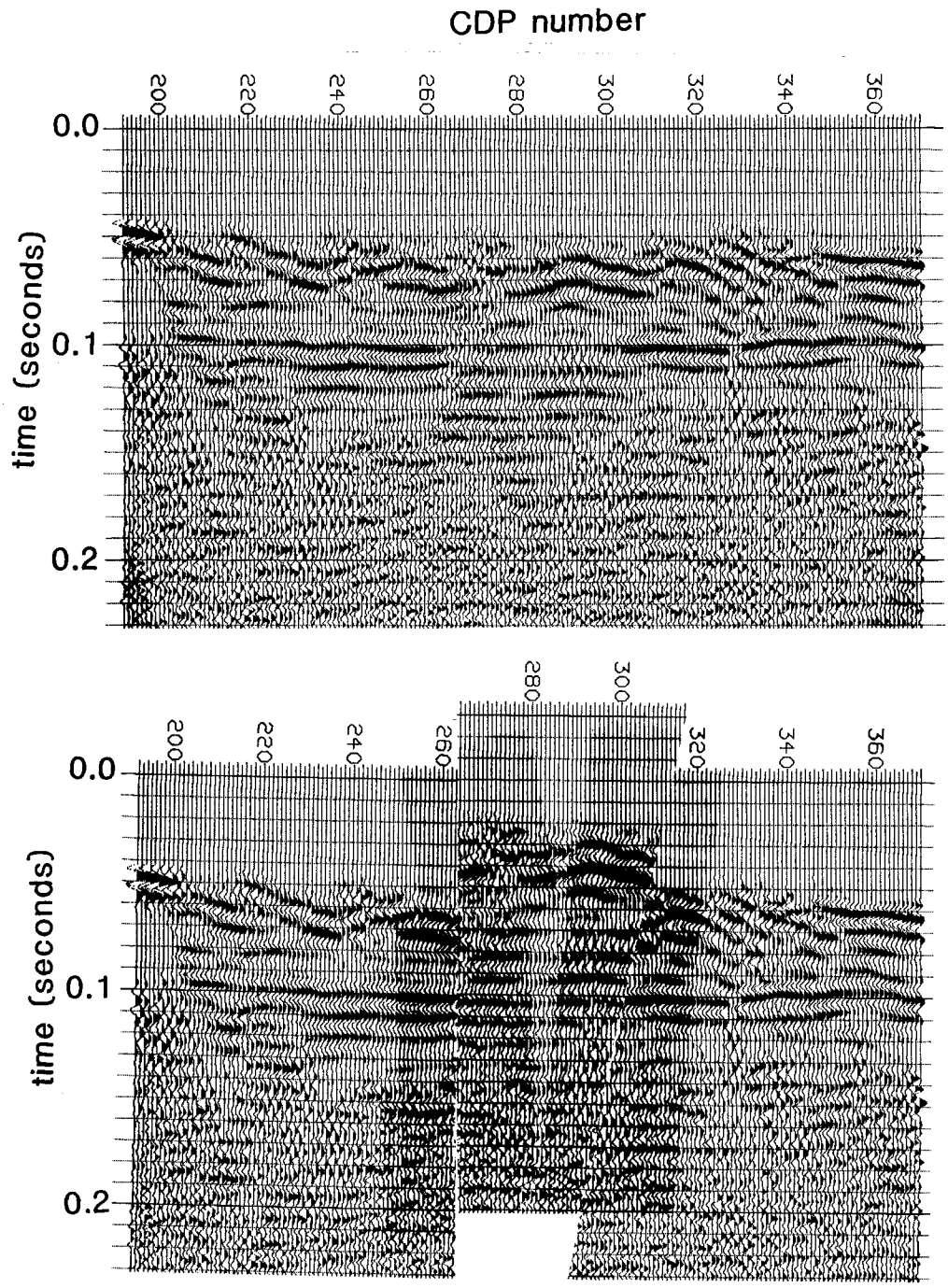
CDP number
200
220
240
260
280
300
320
340
360
0.0
0.1
0.2
time (seconds)
280
300
200
220
240
260
320
340
360
0.0
0.1
0.2
time (seconds)

extensive along these faults, possibly no more than 10 meters.

The reduced amplitude of high frequency events associated with the horizontal oversampling phenomenon discussed in detail for line 1 is also evident on the real-trace stacked section for line 3. The horizontal oversampling phenomena result in the appearance of continuity of reflections across the faulted regions.

All three seismic plots (the real-trace stacked section, the instantaneous phase, and the instantaneous frequency) led to the composite interpretive line drawing (Figure 29). The more prominent reflected events are illustrated in the line drawing, however no conclusive correlation can be achieved across the faulted regions. Detailed stratigraphic control is necessary to correlate beds and quantify displacements. Approximate depth scales displayed on the sides of the interpretive line drawing are derived from stacking velocities ranging from 1250 to 2000 m/s. Faulting dominates the entire extent of the line 3 traverse. Although this is a small sample of data acquired parallel to the scarp, the density of faulting would suggest the possibility of deformation exists (at least locally) along the entire length of the fault scarp.

Figure 29. Interpretive line drawing for seismic line 3 derived from both the real trace and the complex trace sections.

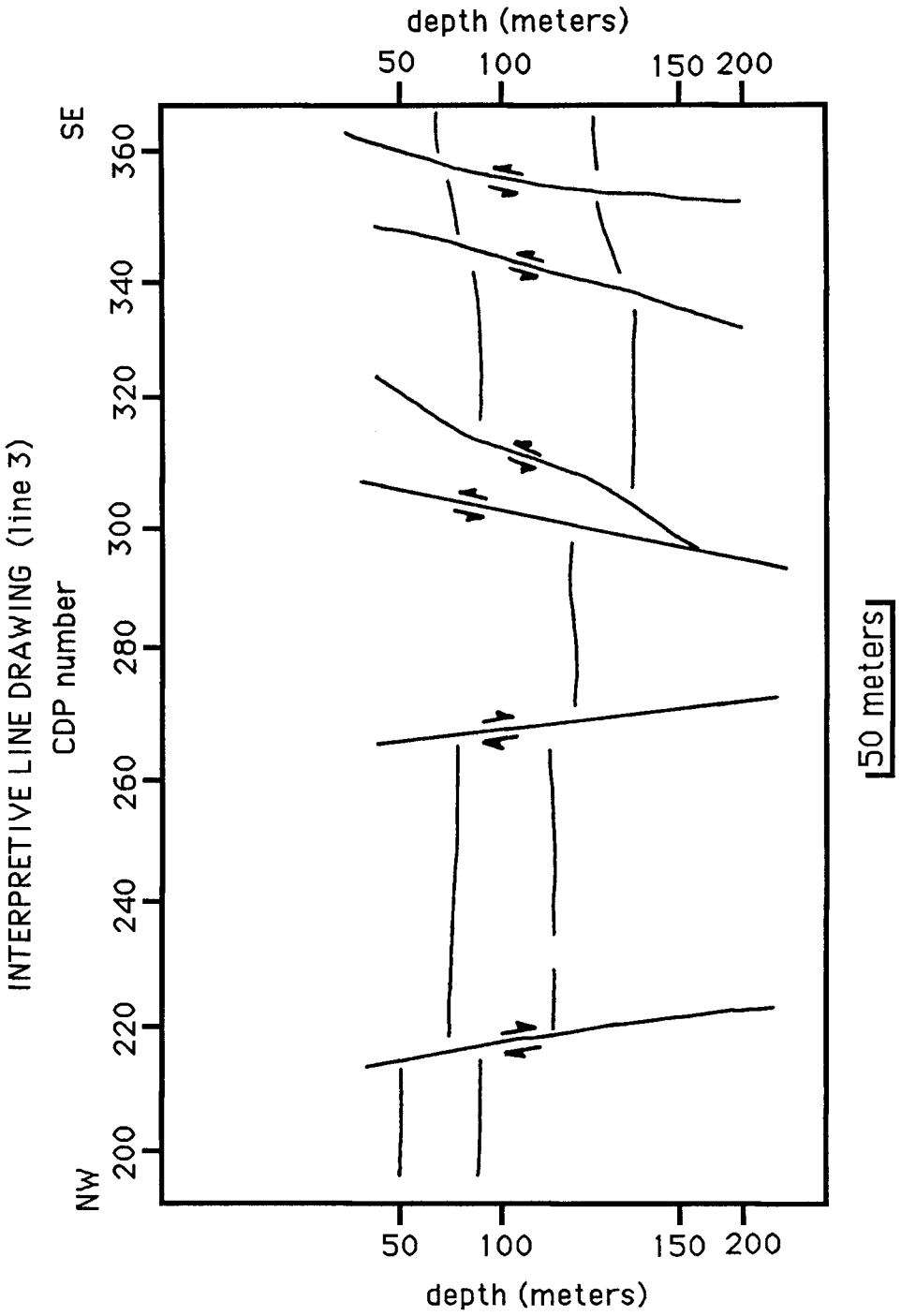
depth (meters)
50
100
150
200
SE
360
340
320
300
280
260
240
220
200
NW
INTERPRETIVE LINE DRAWING (line 3)
CDP number
50 meters
depth (meters)

RESULTS AND CONCLUSIONS

Amplitude, frequency, and wavelet character changes across individually reflected events helped to delineate deformational features and allowed interpretation of seismic sections both perpendicular and parallel to the Meers Fault scarp. Severe analog low-cut filtering during acquisition resulted in recorded frequencies well over 100 Hz. Complex trace attributes, primarily instantaneous phase provided a significant contribution to the overall interpretation of the shallow structure. Combining data from several sources (real trace and complex trace) adds significantly to the validity of the study.

The two seismic traverses running perpendicular to the scarp (line 1 and line 2) provided the information necessary to decipher the shallow structure normal to the fault plane. Data from lines 1 and 2 illustrate the repeatability of seismic surveys and therefore further substantiate the validity of the shallow seismic reflection technique as applied to the study of faulting.

Presence of the major fault associated with the scarp and minor faulting at depths ranging from approximately 30 meters to 200 meters can be observed in the seismic data perpendicular to the fault plane. The presence of faulting on both the northeast and southwest flanks of the fault

suggests that the entire Meers Fault zone extends at least 250 meters to the southwest and at least 200 meters to the northeast of the scarp. However, the majority of deformation appears to be concentrated within 100 meters on either side of the scarp. Movement along the minor faults on both the northeast and southwest flanks appears to be minimal, no more than 10 meters. Correlation of the reflected events across these faults can be accomplished based solely on the seismic character of the reflected events. Correlation of the reflected events across the major fault associated with the scarp is essentially impossible without detailed stratigraphic information that could be obtained by as few as two drill holes, including seismic velocity check shots.

Data from seismic line 3 (parallel to the scarp) display normal dip slip faulting throughout the entire traverse. The most significant feature is a graben (maximum 35 meters displacement) located between CDP 265 and CDP 300. There is no evidence for the graben in the surface expression. The deformation observed parallel to the scarp supports the findings for strike slip motion along the fault. The spatial extent of seismic line 3 only covers a very small sample along the approximately 40 km surface extent of the Meers Fault. However, the random nature in which the line parallel to the scarp was chosen

in conjunction with the spatial frequency at which the faulting occurs along the seismic section suggests that deformation possibly exists along the majority of the Meers Fault's northwest to southeast extent.

All of the data from seismic lines 1 and 2 have illustrated that a predominantly compressive stress has driven the most recent vertical motion. Contrary to the majority of Late-Pennsylvanian Early-Permian significant up-to-the-south displacement, the Quaternary vertical movement appears to be dominated by the reactivation of a Late-Permian fault plane displaying up-to-the-north motion. The nature of the vertical motion in conjunction with the evidence for strike slip motion places the Meers Fault in a transpressive stress environment during Quaternary time.

REFERENCES

Bracewell, R.N., 1965, The Fourier Transform and its Applications. New York, McGraw Hill 268-271.

Brewer, J.A., 1982, Study of Southern Oklahoma Aulacogen, Using COCORP Deep Seismic-Reflection Profiles. Oklahoma Geological Guidebook 21, 31-39.

Butler, K.R., 1980, A Structural Analysis of the North Flank of the Wichita Mountains, Oklahoma. GSA Abstracts with Programs, 12, 2.

Chun, J.H., and Jacewitz, C.A., 1981, Fundamentals of Frequency Domain Migration. Geophysics, 46, 5, 717-733.

Cox, R., and VanArsdale, R., 1986, Style and Timing of Displacement Along the Washita Valley Fault, Oklahoma. GSA Abstracts with Programs, 18, 6, 573.

Crone, A.J., and Luza, K.V., 1986, Holocene Deformation Associated with the Meers Fault, Southwestern Oklahoma. Oklahoma Geological Guidebook 24, 68-74.

Donovan, R.N., and Ragland, D.A., 1986, Paleozoic Stratigraphy of the Slick Hills, Southwestern Oklahoma. Oklahoma Geological Guidebook 24, 13-16.

Donovan, R.N., Sanderson, D.J., and Marchini, D., 1982, An Analysis of Structures Resulting from Left-Lateral Strike Slip Movement Between the Wichita Mountains and the Anadarko Basin, Southwestern Oklahoma. GSA Abstracts with Programs, 14, 476.

Haar, L.A., Fletcher, J.B., and Mueller, C.S., 1984, The 1982 Enola, Arkansas Swarm and Scaling of Ground Motion in the Eastern U.S. Seismological Society of America Bulletin 74, 6, 2463-2482.

Harlton, B.H., 1951, Faults in the Sedimentary Part of the Wichita Mountains of Oklahoma. American Association of Petroleum Geologists Bulletin, 35, 5, 988-999.

Harlton, B.H., 1963, Frontal Wichita Fault System of Southwestern Oklahoma. American Association of Petroleum Geologists Bulletin, 47, 8, 1552-1580.

Harlton, B.H., 1972, Fault Fold Belts of the Southern Anadarko Basin Adjacent to the Frontal Wichitas. American Association of Petroleum Geologists Bulletin, 56, 8, 1544-1551.

Hunter, J.A., Pullan, S.E., Burns, R.A., Gagne, R.M., and Good, R.L., 1984, Shallow Seismic Reflection Mapping of the Overburden-Bedrock Interface with the Engineering Seismograph-Some Simple Techniques. Geophysics, 49, 8, 1381-1385.

Knapp, R.W., and Steeples, D.W., 1986, High Resolution Common Depth Point Seismic Reflection Profiling:Field Acquisition and Parameter Design. Geophysics, 51, 283-294.

Mayne, W.H., 1962, Common-Reflection-Point Horizontal Data-Stacking Techniques. Geophysics, 27, 927-938.

McLean, R., and Stearns, D.W., 1983, Fault Analysis in the Wichita Mountains. American Association of Petroleum Geologists Bulletin, 67, 511-512.

Miller, R.D., and Steeples, D.W., 1986, Shallow Structure from a Seismic Reflection Profile Across the Borah Peak, Idaho Fault Scarp. Geophysical Research Letters, 12, 9, 953-956.

Pullan, S.E., and Hunter, J.A., 1985, Seismic Model Studies of the Overburden-Bedrock Reflection. Geophysics, 50, 11, 1684-1688.

Ramelli, A.R., and Slemmons, D.B., 1986, Neotectonic Activity of the Meers Fault. Oklahoma Geological Guidebook 24, 45-54.

Ramelli, A.R., Slemmons, D.B., and Brocoum, S.J., 1987, The Meers Fault: Tectonic Activity in Southwestern Oklahoma. U.S. Nuclear Regulatory Commission, NUREG/CR-4852.

Sheriff, R.E., 1984, Encyclopedic Dictionary of Exploration Geophysics. Society of Exploration Geophysicists, Tulsa, 208.

Slemmons, D.B., Ramelli, A.R., and Brocoum, S.J., 1985, Earthquake Potential of the Meers Fault. Earthquake Notes, 55, 1.

Steeples, D.W., Miller, R.D., and Knapp, R.W., 1987, Downhole .50 Caliber Rifle-An Advance in High

Resolution Seismic Sources. Technical Program Abstracts and Biographies, SEG, 57th Annual Meeting.

Taner, M.T., Koehler, F., and Sheriff, R.E., 1979, Complex Seismic Trace Analysis. Geophysics, 44, 1041-1063.

Taner, M.T., and Sheriff, R.E., 1977, Application of Amplitude, Frequency, and other Attributes to Stratigraphic and Hydrocarbon Determination: in Payton, , C.E., Ed., Applications to Hydrocarbon Exploration. AAPG Memoir 26, American Association of Petroleum Geologists, 301-327.

Treadway, J.A., Steeples, D.W., and Miller, R.D., 1985, Seismic Reflections Within the Upper 100 Feet Near Borah Peak Idaho, Earthquake Scarp. Technical Program Abstracts and Biographies, SEG 55th Annual Meeting, 161-163.

Widess, M.B., 1973, How Thin is a Thin Bed? Geophysics, 38, 1176-1180.

Zoback, M.L., and Zoback, M.D., 1980, State of Stress in the Conterminous United States. Journal of Geophysical Research, 85, b11, 6113-6156.

APPENDIX A: Stratigraphy of Southwestern Oklahoma.

The majority of the stratigraphic information contained in APPENDIX A is summarized from:

Donovan, R.N., and Ragland, D.A., 1986, Paleozoic Stratigraphy of the Slick Hills, Southwestern Oklahoma. Oklahoma Geological Guidebook 24, 68-74.

The Timbered Hills Group marks the introduction of the Paleozoic record in the Wichita Mountains, Anadarko Basin area. Pre-Timbered Hills topography consisted of small hills of rhyolite reaching approximately 100 m high. These hills were part of the Carlton Rhyolite Group forming the upper part of the basement igneous complex and acted as a source of rhyolite detritus within the Reagan Sandstone, the lowest formation of the Timbered Hills Group.

The Reagan Sandstone was deposited during the Cambrian transgression. It is the only formation in the Timbered Hills group dominated by siliciclastics and is composed primarily of interbedded sandstones and minor shales. The sandstone is dominated by quartz with some rhyolite clasts. Typically, the Reagan is split into three members. The lower most member consists of a fine-grained, purple-brown, quartz-hematite, cemented sandstone that exhibits a significant amount of medium scale cross-bedding. The upper Reagan was deposited in still waters and is composed

of a light brown sandstone cemented by quartz and may contain up to 55% glauconite at the formation boundary. Cross-bedding is also abundant in the Upper Reagan, however, at a slightly larger scale.

The Honey Creek Formation represents the top of the Timbered Hills Group and consists of carbonate rocks. The lower formation contact is recognized by its distinctive orange weathering zone. This zone is produced by a diagenetic reaction between the glauconite in the Upper Reagan and the carbonate of the lower Honey Creek. The limestones of the Honey Creek Formation are well-washed, cross-bedded, bioclastic grainstones dominated by pelmatozoans, lesser amounts of thick shelled trilobites, and orthid brachipods. They may be contaminated by varying amounts of quartz, glauconite, rhyolite, and phosphatic shell grains. As with the Reagan, the Honey Creek can be split into three members, a lower and upper carbonate member sandwich a fine grained, calcareous quartz arenite that may reach a thickness of approximately 40 feet.

The Cambro-Ordovician Arbuckle Group overlies the Timbered Hills Group. The Arbuckle consists of muddy carbonates. Simple gravity settling dominates sedimentation throughout the Arbuckle. Sediments are poorly washed resulting in an abundance of wackestones and mudstones. Intraformational conglomerates are also

recognized throughout the Arbuckle, with an abundance of chert appearing near the upper part of the group. The Arbuckle is divided into six formations beginning with the Fort Sill Formation in late Cambrian time and continuing through the West Spring Creek Formation in Ordovician time.

The Fort Sill Formation consists of three basic units. The basal unit is a thin-bedded limestone sequence dominated by mudstones. The middle sequence consists of alternating lime mudstones and dolomite siltstones. The upper sequence is a more massive limestone containing algal boundstones. The contact between the Fort Sill and the Signal Mountain Formations is easily recognized by the consistently thin-bedded nature of the Signal Mountain Formation.

The Signal Mountain formation marks the Cambrian-Ordovician boundary. It is recognized as the most consistently thin-bedded limestone formation in the Arbuckle Group. Recognizing the Upper boundary of the Signal Mountain Formation is extremely difficult.

The base of the Mckenzie Hill Formation is difficult to place but is marked by its lack of chert. The upper McKenzie Hill is abundant in chert.

The Cool Creek Formation is the most varied formation in the Arbuckle Group. It consists of algal boundstones interbedded with intraformational conglomerates and

breccias, oolite limestones, micrites, evaporite-pseudomorph-bearing dolostones and quartz-rich sandstone. The Thatcher Creek member is a basal quartz sand representing the first silicous detritus in the Arbuckle Group.

The Kindblade Formation is characterized by the Gastroped genus Ceratopea. Overall, the Kindblade Formation is very similar to the Cool Creek except the bed thicknesses are greater and evaporitic dolomites are uncommon.

The West Spring Creek Formation is recognized by a basal sandstone unit similar to the Thatcher Creek member in the Cool Creek Formation. The formation is very similar to the Kindblade and Cool Creek except it is the only unit in the Arbuckle Group that contains graptolites.

Resting unconformably on the Arbuckle Group is the Hennessey Group of Permian age. Permian red beds and in some places the Post Oak Conglomerate unit mark the top of the existing Paleozoic record. Figure 30 illustrates the ages of the stratigraphic units in southwestern Oklahoma.

Madole (1986) recognized five major Quaternary alluvial deposits over the Meers Fault. The deposit that is significant to this study he terms the Porter Hill Alluvium which ranges in thickness from 2.3 m to 3.9 m. The Porter Hill is predominantly gravel capped by a thin

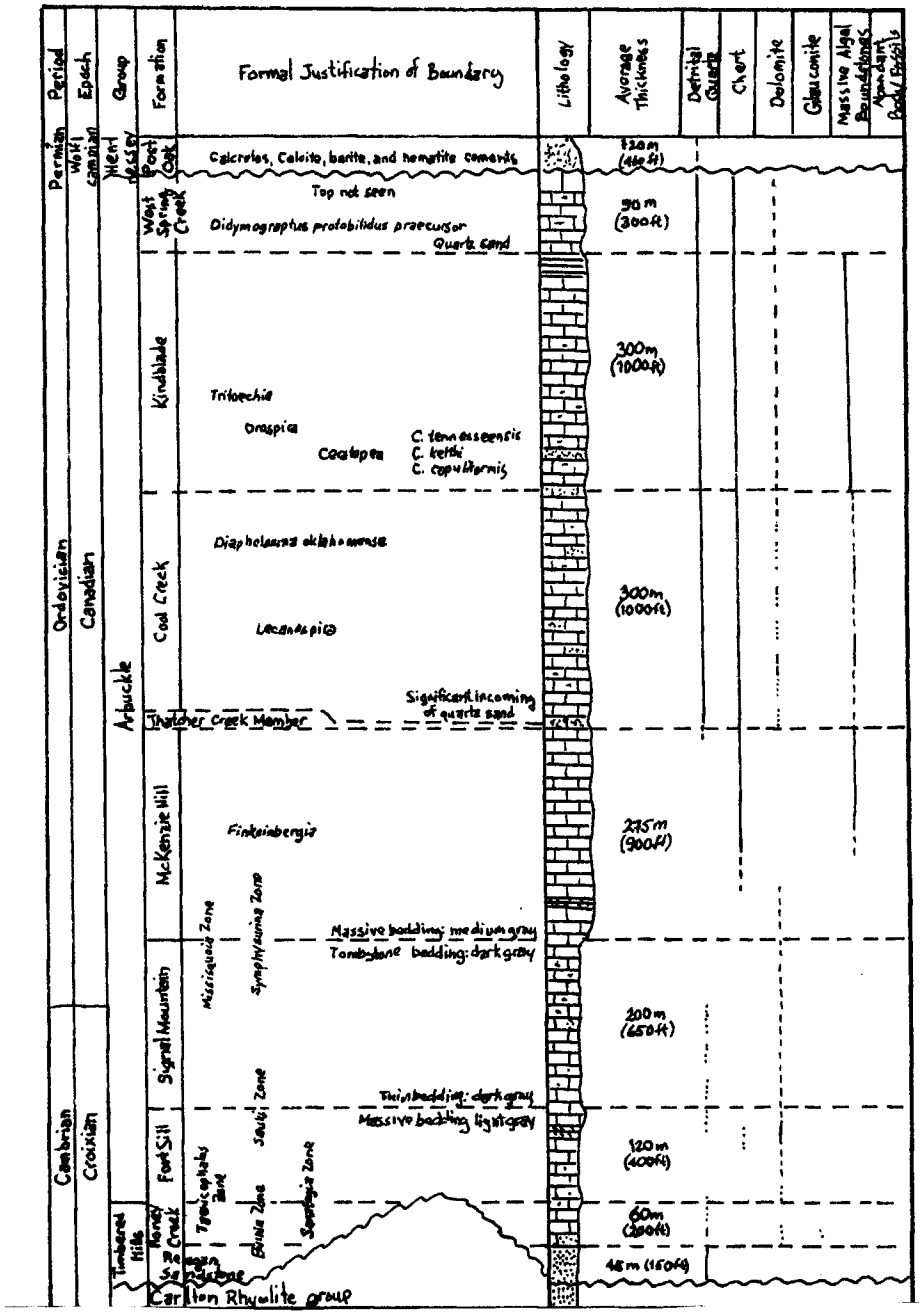

Figure 30. Stratigraphic section of southwestern Oklahoma. (from Donovan and Ragland, 1986).

veneer of finer sediments approximately .5 m thick. The gravel consists of 25-40% clasts of pebbles, small and large cobbles, and a few boulders in a red clay matrix. Madole believes the Porter Hill Alluvium was deposited during middle Pleistocene time approximately 290,000 to 130,000 years before the present.

APPENDIX:B Data Acquisition Parameters

		line 1	line 2	line 3
Recording system		Input/Output DHR-2400 24 Channel		
Record Length		250ms	250ms	250ms
Sample Interval		0.5ms	0.5ms	0.5ms
Analog Filters	lo-cut	220	110	110
	hi-cut	1000	1000	1000
Source		Downhole .50-Caliber Rifle		
Source Spacing		8 ft.	2 m	2 m
Receivers		Two 100-Hz Geophones in Series		
Receiver Spacing		4 ft.	2 m	2 m
Source to Closest Receiver				
		29.3 m 30.5 m	10 m	10 m
Geometry		End-on	Pseudo Split Spread	End-on
Nominal CDP Fold		12	24	12

APPENDIX C: Data Processing

Statics 1.elevation shot/receiver
2.automatic surface consistent

Muting 1.first arrival mute for line 1
2.air-wave mute lines 1, 2, 3.

Deconvolution
autopredictive 1.2nd zero-crossing
for line 3.

Trace editing

CDP-sorting

Velocity functions

	CDP	time (ms)	velocity m/s
line 1	176-299	40	1370
		65	1525
		85	1750
	300-362	60	1300
		70	1750
	363-415	70	1300
		80	1675
		120	2000
line 2	270-379	95	1100
		110	1800
	380-419	95	1200
		110	1800
	420-429	95	1400
		110	1800
	430-479	100	1800
		160	2400
	480-489	80	1500
		100	1800
		150	2000
	490-549	80	1100
		150	1500
	550-559	100	2000

	560-599	100	1500
		140	2000
	600-620	120	1800
		140	2000
line 3			
	192-370	70	1250
		90	1750
		180	2000

Filters (bandpass with filter length = 60ms)

line 1,3

100% points	90, 250
0% points	45, 375

line 2 (time varying)

above 110 ms:	
100% points	90, 200
0% points	45, 300
below 110 ms	
100% points	70, 150
0% points	35, 225

Scaling (for visual)

AGC	window length.
line 1	50 ms
line 2	20 ms
line 3	40 ms

APPENDIX D: Complex Trace Analysis

Seismic waves which are detected by geophones and recorded in the field can be thought of as an analytic signal that possesses both real and imaginary parts (figure 31). The seismic trace, $f(t)$, which is typically displayed is the real component of the analytical signal or complex trace, $F(t) = f(t) + \mathrm{if}^*(t)$ (Taner, et al., 1979). The imaginary component of the analytic signal, $f^*(t)$, is referred to as the quadrature trace and can be generated from the observed real trace through Hilbert transform techniques (Bracewell, 1965). Physically, the complex trace can be thought of as a separation of kinetic and potential energy (Taner and Sheriff, 1977). The seismic trace, or real component, is a measure of the velocity of motion which result from the passage of seismic energy and therefore involves kinetic energy. According to Taner and Sheriff (1977) the particle motion is resisted by an elastic restoring force so that energy becomes stored as potential energy. As the particles move in response to a passage of the seismic waves, the energy switches back and forth between kinetic and potential forms. The quadrature trace, $f^*(t)$, may be thought of as a measure of the potential energy.

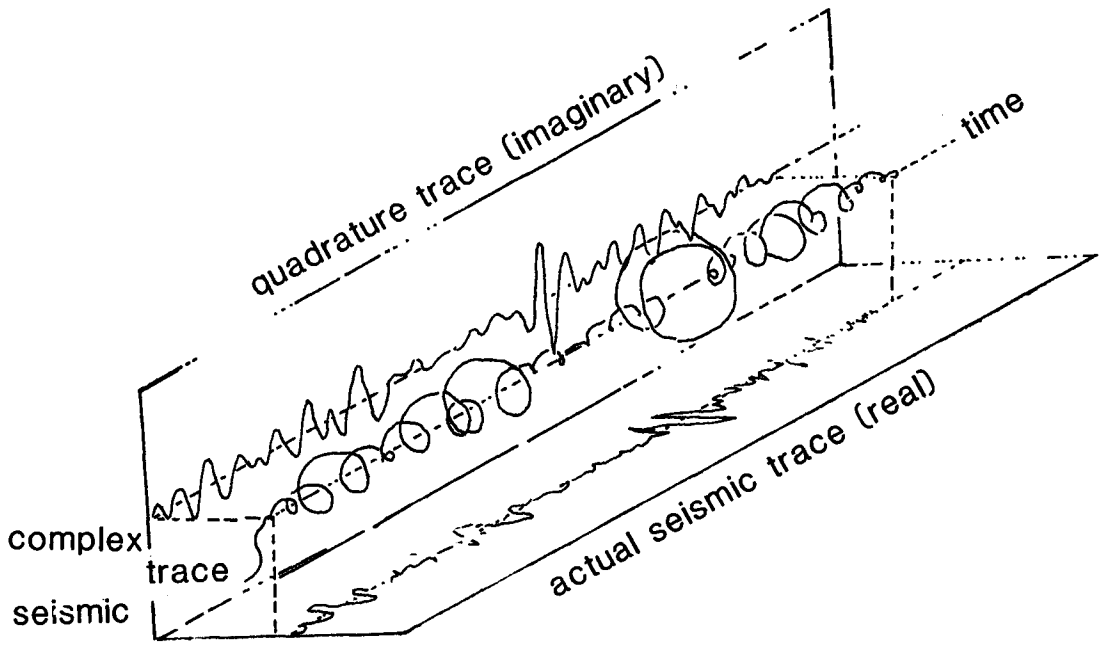

Figure 31. Representation of the complex seismic trace. (from Taner et al. 1979).

The real seismic trace can be expressed in terms of a time-dependent amplitude $R(t)$ and a time dependent phase $\theta(t)$, such that:

$$f(t) = R(t)\cos\theta(t)$$

The quadrature, or imaginary trace is therefore given by:

$$f^*(t) = R(t)\sin\theta(t)$$

The complex trace, $F(t)$, is the sum of the real and imaginary traces resulting in:

$$F(t) = f(t) + \text{if}^*(t) = R(t)e^{i\theta(t)}$$

Using the complex trace $F(t)$ allows us to define instantaneous amplitude, (also known as the reflection strength) instantaneous phase and instantaneous frequency. The additional information obtained from these three attributes significantly aids in the interpretation process of seismic data.

The Reflection strength is obtained by taking the magnitude of the complex trace:

$$Rt = (f(t)^2 + f^*t^2)^{1/2} = |F(t)|$$

Reflection strength is independent of phase and therefore may have its maximum at phase points other than peaks or troughs of the real seismic trace. According to Taner et al., (1979) high reflection strength is indicative of major lithologic changes between adjacent rock layers.

The instantaneous phase $\theta(t)$ attribute is obtained by taking the inverse tangent of the quadrature trace divided by the real trace.

$$\theta(t) = \tan^{-1}[f^*(t)/f(t)].$$

The instantaneous phase emphasizes the continuity of events. Instantaneous phase is independent of reflection strength and therefore makes weak coherent events more clear. As a result, this attribute is effective in showing discontinuities, faults, pinchouts, angularities, and events with different dip attitudes which interfere with each other (Taner et al., 1979).

Instantaneous frequency is obtained by taking the rate of change of the instantaneous phase.

$$\frac{d\theta(t)}{dt} = \omega(t)$$

Similar to instantaneous phase, instantaneous frequency is a value associated with a point in time. Typically reflection events may represent a composite of individual reflections from a number of closely spaced reflectors. This superposition may produce a frequency pattern which characterizes the composite reflection. Therefore, instantaneous frequency plot may be useful as a correlation tool.

The three complex trace attributes mentioned above are typically displayed with color. The usual color-encoding of reflection strength is referenced to the maximum reflection strength from the seismic section, using a different color for each db step. Instantaneous phase displays use a color wheel such that plus and minus 180 degrees are the same color because they are the same phase angle. Instantaneous frequency is usually colored in 2 Hz steps.

Three complex trace attributes used together can be a significant contribution to the interpretation process of a seismic study. However, for a fault study, as this project illustrates, the instantaneous phase attribute is most applicable.

APPENDIX E: MIGRATION

Zero-offset reflection events as on a stacked seismic section will give the appearance that the recorded energy traveled vertically down to the reflecting horizon and back to the receiver. However, in the case of a dipping reflecting horizon, this is not valid. Consequently, data recorded from a dipping reflector are spatially distorted.

To illustrate this distortion, consider a segment from a dipping reflector CD in a depth section (Figure 32A). Converting to a zero-offset time profile along OX results in a repositioning of segment CD to segment C'D' oriented vertically under their respective shot points A, B (Figure 32B). Comparing the zero-offset time section with the actual depth section reveals:

1. The dip angle of the reflector in the geologic section is greater than the time section.

2. The length of the reflector seen in the geologic section is shorter than the time section.

3. The geologic section is up-dip from the time section.

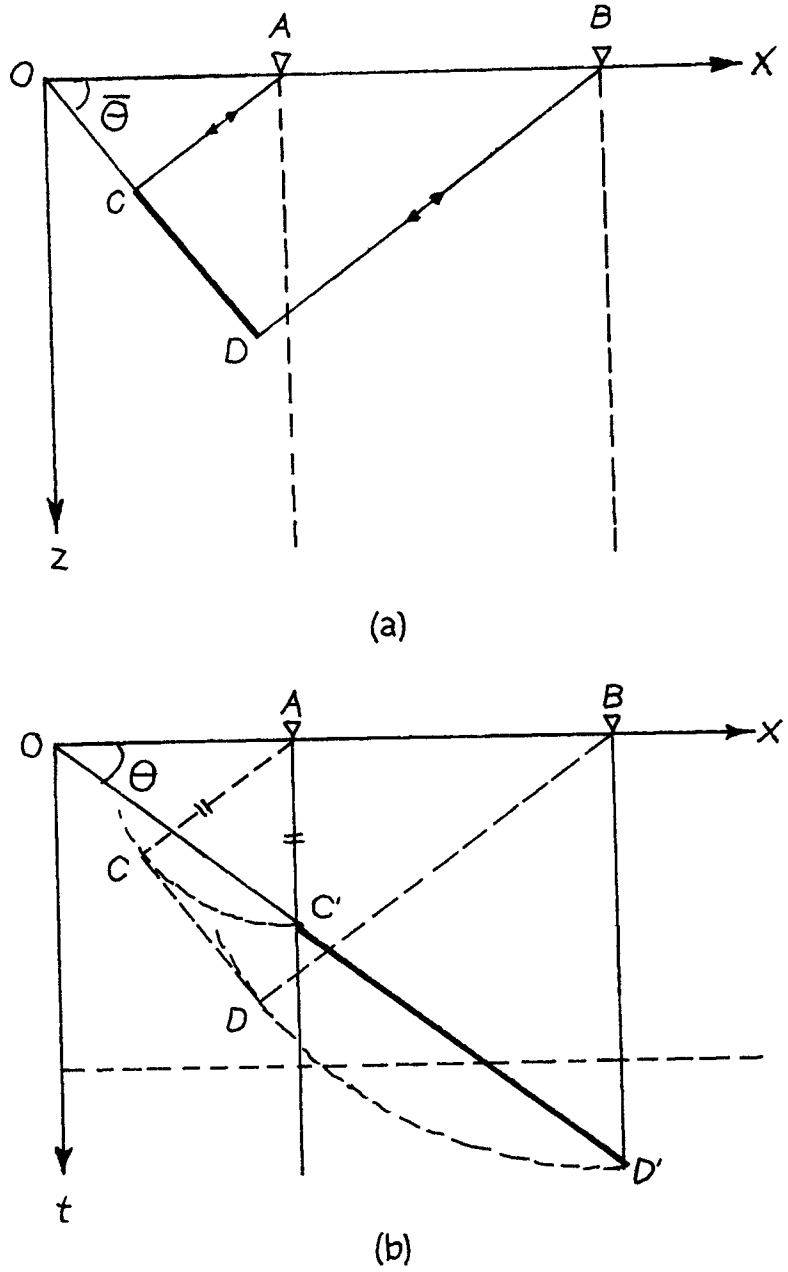

Figure 32. Migration of a segment of a dipping event. (from Yilmaz, 1987).

Migration of seismic data is a process of mapping one time section onto a 2nd time section in which events are repositioned to their actual location in space. The process moves dipping reflectors in to their time subsurface positions and collapses diffractions back to a single point. The goal of migration is to make to stacked seismic section appear similar to the actual geologic cross-section. The three major techniques of migration commonly used are diffraction or Kirchoff integral migration, finite-difference migration, and frequency domain or $f-k$ migration. Frequency domain or $f-k$ migration was the technique used in this study and will be the only type discussed.

A flow chart for performing the $f-k$ migration technique is illustrated in figure (33). The first step involves converting a zero-offset seismic section in the xt plane, (x = distance, t = time), to the $k_x\omega$ plane, (k_x = horizontal wavenumber, ω = temporal frequency = $2\pi f$). This is accomplished using a 2D Fourier transform. Dipping events in the xt plane will plot perpendicular to the dipping events in the $k_x\omega$ plane (Figure 34). Therefore, all dip information is preserved in the transformation. All events in the xt plane possessing the same dip will plot on the same line in the $k_x\omega$ plane thereby minimizing the complexity of the record.

Figure 33. Flow chart for $f - k$ migration. (from Yilmaz, 1987).

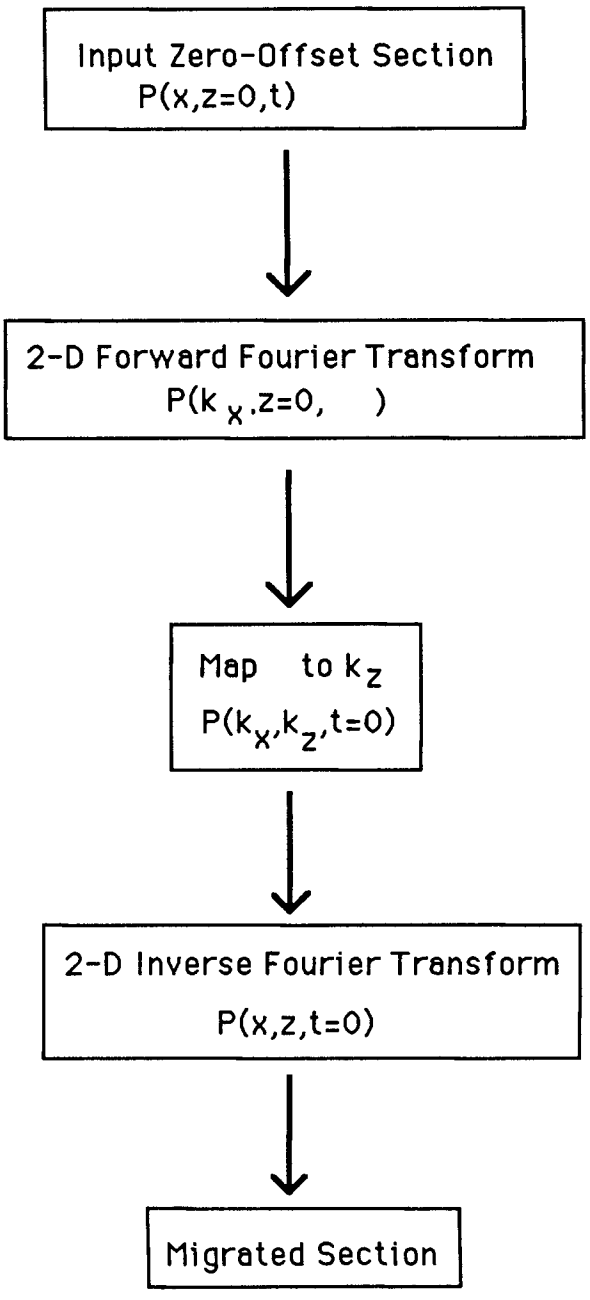
Input Zero-Offset Section
P(x,z=0,t)
2-D Forward Fourier Transform
P(k x.z=0,)
Map to k z
P(k x,k z,t=0)
2-D Inverse Fourier Transform
P(x,z,t=0)
Migrated Section

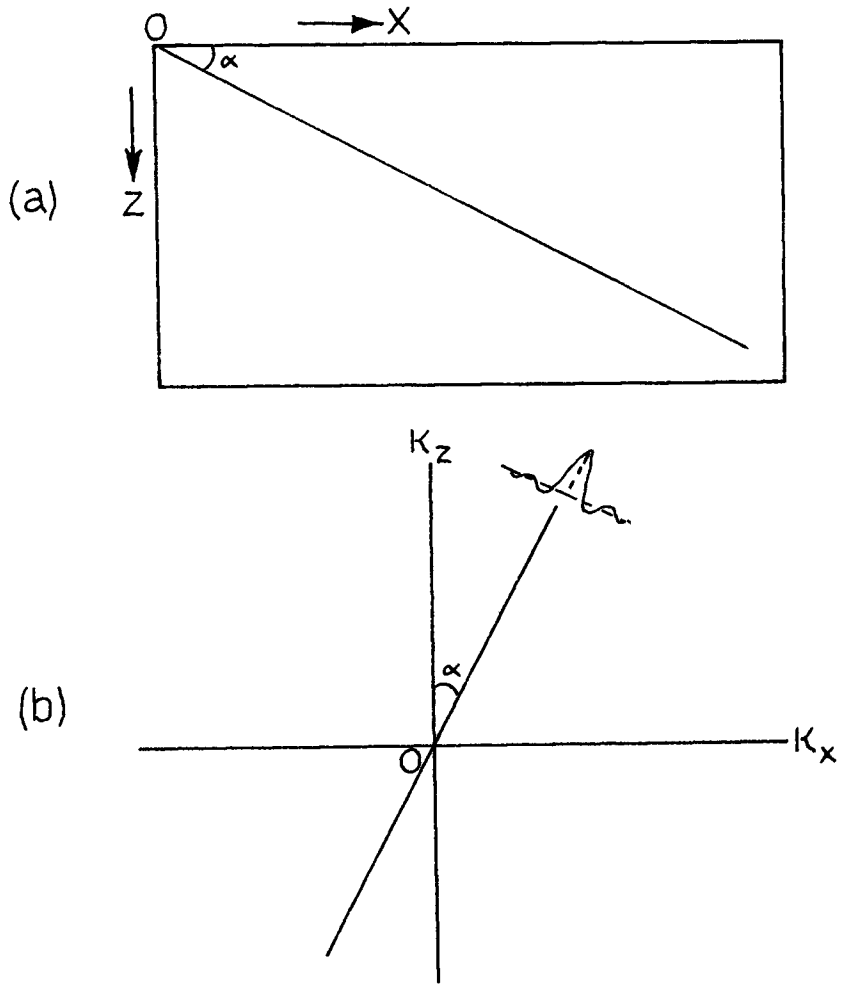

Figure 34. 2D Fourier Transform to the $f - k$ plane. (from Yilmaz, 1987).

Migration of the dipping events converts the data from the $k_x\omega$ plane to $k_z k_x$ plane (k_z =vertical wavenumber), by repositioning the event to its actual location. The procedure is illustrated in figure 35 and involves:

1. Drawing a circle whose radius is equal to OA (A is an arbitrary point on the k_z axis). The center is located at 0.

2. Draw a horizontal line from A until it intersects the dipping event .

3. Draw a vertical line from point B and find the intersecting point with the circle (B').

4. Draw a line that passes through the origin and point B'.

The result is the migrated dip line.

The final step in the procedure is the 2D inverse Fourier transform back to the xt plane. The result is a geologic section with events possessing steeper dip angles than the unmigrated section. The relationship between the unmigrated dip angle (θ) and the migrated dip angle ($\bar{\theta}$) is given by:

$$\sin\theta = \tan\bar{\theta}$$

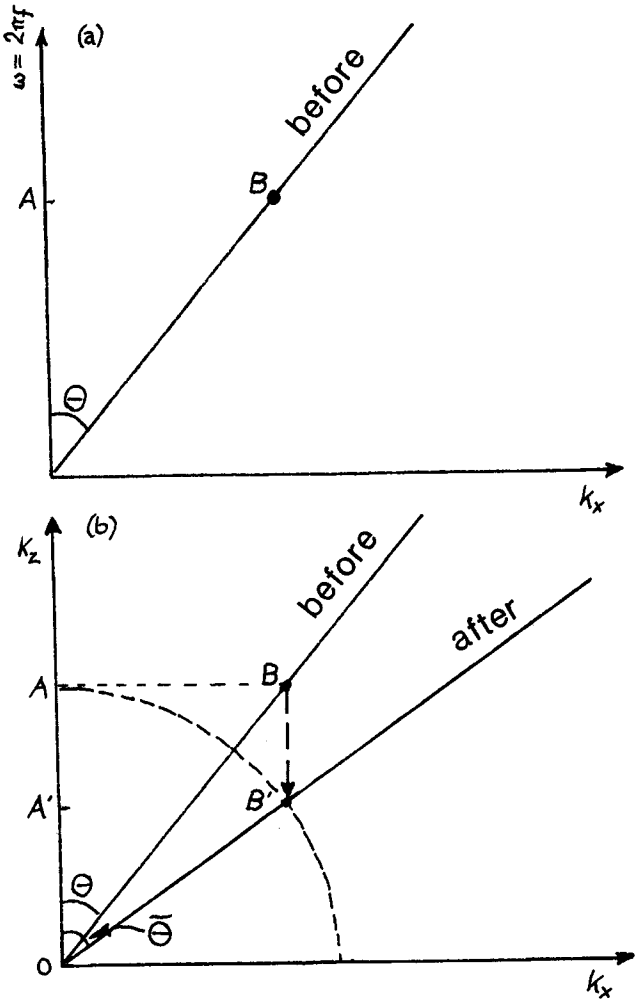

Figure 35. Procedure for $f - k$ migration. (from Yilmaz, 1987).

According to Chun and Jacewitz (1978) the advantages of ($f-k$) migration include fast computation time, good performance under low signal-to-noise ratio, and excellent performance for steep dips. Difficulties arise when a widely variable velocity function is used. For more detailed mathematics on ($f-k$) migration the reader is referred to Yilmaz (1987).

Frequency domain ($f-k$) migration was performed on the stacked seismic section for line 1 in this study (Figure 36). Similar features can be seen on the migrated section as the unmigrated section despite extremely poor migration results. Pre-migration data possessed minimal dip, minimizing the importance of the migration process. The poor data quality post-migration was not terribly surprising considering Chun and Jacewitz (1978) mention of difficulties with a widely varying velocity function. The velocity function for line 1 ranges from 1300 m/s to 1830 m/s in just 90 ms of data. The $f-k$ migration software available for this project allows for a single velocity input. The velocity chosen was for figure (36) was 1400 m/s. Consequently, migration was not performed on line 2 or line 3.

Figure 36. $f-k$ migrated section for line 1.

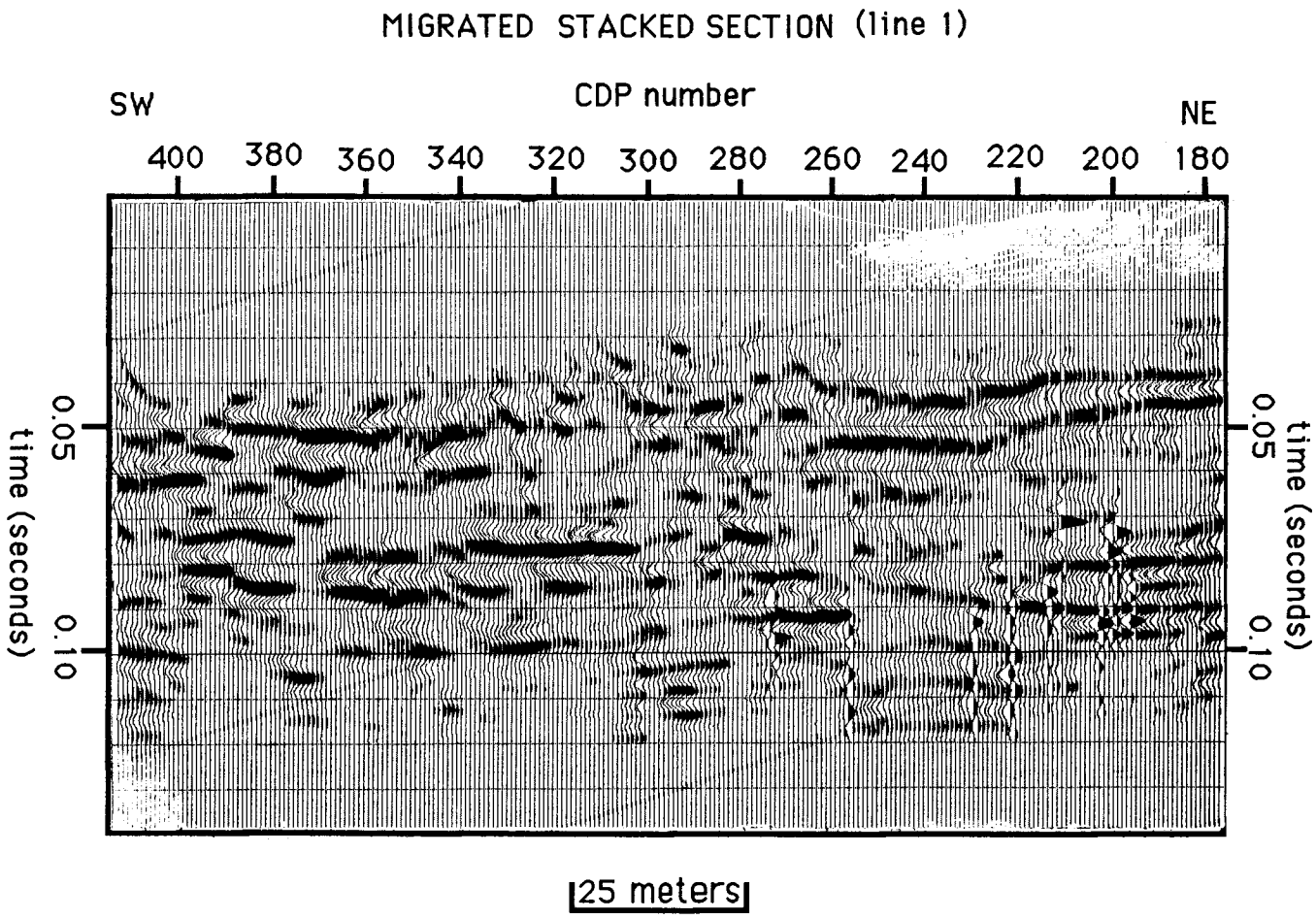
MIGRATED STACKED SECTION (line 1)
SW
CDP number
NE
400 380 360 340 320 300 280 260 240 220 200 180
0.05
0.10
time (seconds)
0.05
0.10
time (seconds)
25 meters